Pre-printed version of the paper published in the journal: International Journal for Numerical Methods in Engineering, Vol. 93, pp1314-1344, 2013

An XFEM plate element for high gradient zones resulted from yield lines

Jin Xu, C.K. LEE, K.H. TAN

School of Civil & Environmental Engineering, Nanyang Technological University, Singapore

xu0003in@e.ntu.edu.sg

Summary

A high gradient of displacement field occurs when a yield line is formed in a plate with elasto-plastic material. For such applications, the Extended Finite Element Method (XFEM) has shown to be an effective numerical method to capture the behavior of a plate with a locally non-smooth displacement field, as well as a displacement field with a high gradient. In this article, a 6-node isoparametric plate element with XFEM formulation is presented to capture the elasto-plastic behavior of a plate in small-deformation analyses. The Hermite function is adopted at the element level to enrich both the translational and the rotational displacement approximation fields so that non-smoothness in displacement fields near a yield line can be simulated.

Key words: extended finite element method, regularized shifted enrichment, Hermite function, plate element, yield line

1 Introduction

When a yield line forms in a plate, rapid changes in rotational fields and in the gradients of deflection fields occur within a short range, as shown in Figure 1. The rapid changes make the displacement field non-smooth locally near the yield line. During the failure analysis of a plate in a bending-dominant case, a point at the extreme layer of the plate yields when the effective stress at that point reaches the yield strength of the material. With increasing loading, more material points in the plate reach yield. The yielded zone extends to the middle layer in the thickness direction and also spreads to the nearby area. A yield line forms when a continuous area has yielded and a plastic mechanism forms when sufficient yield lines coalesce together in the plate. After the plastic mechanism has formed, loading cannot be further increased and the plate may eventually collapse. During the above yielding and collapsing process, the non-smoothness characterized from the yield line becomes apparent as the load level increases gradually. Different from a discontinuity such as a crack in a plate, this non-smoothness appears within a finite dimension. Therefore, this non-smoothness due to yield lines is usually associated with the term 'high gradient' [1].

In a standard finite element analysis, an accurate prediction of the behavior of a plate with elasto-plastic material requires a fine mesh around a yield line. Thus, a large amount of computational effort is needed. Compared to conventional FEM, extended finite element method (XFEM) offers great advantages to model non-smooth physical phenomena. In an XFEM analysis, special functions, which can describe the locally non-smooth displacement field based on a *priori* knowledge, are added into the displacement approximation field. These special functions are called the *enrichment functions*.

The XFEM is first proposed by Belytschko and Black [2] and Moës *et al.* [3] to model crack growth inside a plane element. A crack inside a plane element is regarded as a discontinuity with zero length. The Heaviside function, which generates a strong discontinuity in a displacement field, is added into the displacement approximation field as an enrichment to model the crack development. Sukumar *et al.* [4] introduced a level set function, which is discontinuous in a displacement gradient field, to model a weak discontinuity inside an element. Zi and Belytschko [5] and Moës [6] proposed a shifted enrichment to the displacement field so that the enrichment is non-zero over the domain of interest, which is only a small portion of the whole physical domain. Arias and Belytschko [7] adopted a hyperbolic tangent function as shear band enrichment, which varies rapidly in one direction and slowly in the other, to model shear band growth.

Rabczuk *et al.* [8] and Rabczuk and Samaniego [9] employed strong discontinuous enrichment to model the behavior of a shear band. Benventi *et al.* [10] adopted a regularized model for discontinuity with a conspicuous finite length. Up to now, many efforts have been done on engineering applications of the XFEM such as propagations of cracks [11-13], dislocations [14], interfaces of two different materials [4], the estimation of natural frequency of cracked FGM plates [15], linear buckling analyses of cracked plates [16] and plastic hinges [17]. Some major research works on the PU-enriched shell formulations were reported in [18-21].

In this paper, the XFEM formulation is applied to elasto-plastic plate bending analyses. The XFEM formulation is based on a C_0 plate element. The rotational and the translational displacement approximation fields are enriched simultaneously. Different from the research work on the application of the XFEM in shear band analyses in [8, 9], in the present formulation, the length of the non-smooth zone is not idealized as zero. The regularized enrichments are used instead of the standard strong and weak discontinuous enrichments to capture the local behaviour of a plate with high gradient displacement fields near a yield line. The jump in the strong discontinuous function and the kink in the weak discontinuous function are replaced by a continuous but non-smooth surface with a finite range. The non-smooth surface is formulated by the Hermite function and the range is defined as High Gradient Zone (HGZ). The regularized ‘strong discontinuous’ function is added into the rotation displacement field, while the regularized ‘weak discontinuous’ function is added into the deflection displacement field. Since the Hermite function is used over the HGZ, the enrichments are C_1 continuous *inside* an enriched element. Thus, the strain field is continuous inside an enriched element.

Shear locking phenomenon is studied in the numerical example. A simple reduced Gaussian integration scheme is employed to circumvent the shear locking phenomenon. Since the Hermite function is a polynomial, it is feasible to control the accuracy and the convergence rate of the reduced integration scheme.

As regularized enrichments are used in the present work, the partition of an enriched element could be complex. The complexity of the partition of an enriched element is also discussed in this paper. As a first attempt to solve the elasto-plastic plate analysis, the application of the proposed element is restricted to simple plate structures.

The content of this paper is structured as follows: the governing equation is shown in Section 2. In Section 3, the enrichments for the translational and rotational displacements are introduced. The formulation of a conventional thick triangular plate bending element is described in Section 4. The XFEM element formulation is presented in Section 5, whereas the implementation of the XFEM formulation is discussed in Section 6. Three examples are given in Section 7 to show the effectiveness of the proposed enrichments, followed by conclusions and discussions in Section 8.

2. Governing equation

As shown in Figure 2, the plate structure domain Ω is bounded by Γ. The traction $\overline{\mathbf{t}}$ is defined on the boundary Γ_t and the displacement $\bar{\mathbf{u}}$ defined on the boundary Γ_u. The sub-domain Ω_{ns} denotes the high gradient zone. Given the spaces

$$\mathcal{U}_0 = \{\mathbf{u} \in C_0,\ \mathbf{u} = 0 \text{ on } \Gamma_u,\ \mathbf{u} \text{ is of high gradient within } \Omega_{ns}\} \tag{1}$$

and

$$\mathcal{U} = \{\mathbf{u} \in C_0,\ \mathbf{u} = \bar{\mathbf{u}} \text{ on } \Gamma_u,\ \mathbf{u} \text{ is of high gradient within } \Omega_{ns}\} \tag{2}$$

The equilibrium equation is solved by finding u $\in \mathcal{U}$,

$$\int_\Omega \boldsymbol{\varepsilon}(\mathbf{v})^T \cdot \boldsymbol{\sigma}(\boldsymbol{\varepsilon}(\mathbf{u}))\mathrm{d}\Omega - \int_\Omega \mathbf{g} \cdot \mathbf{v}\mathrm{d}\Omega - \int_{\Gamma_t} \overline{\mathbf{t}} \cdot \mathbf{v}\mathrm{d}\Gamma = 0\,,\ \forall \mathbf{v} \in \mathcal{U}_0 \tag{3}$$

where $\boldsymbol{\sigma}$ is the Cauchy stress and $\mathbf{g}$ is the body force. Small strain assumption is employed and the strain $\boldsymbol{\varepsilon}$ is expressed as

$$\boldsymbol{\varepsilon} = \nabla_s \mathbf{u} \tag{4}$$

where ∇_s is the symmetric gradient operator.

$$\nabla_s \mathbf{u} = \frac{1}{2}\left(\nabla \cdot \mathbf{u} + \mathbf{u} \cdot \nabla\right) \tag{5}$$

The constitutive relationship is

$$\boldsymbol{\sigma} = \mathbf{C}\boldsymbol{\varepsilon} \tag{6}$$

where **C** is the material matrix.

3. The enrichment functions

The rotational displacement field varies rapidly in the direction normal to a yield line, so the enrichment for rotation is a function changing its sign within a small length in that direction. On the other hand, the enrichment for the translational displacement is a function with a rounded transition instead of a kink in the original *level set function* [4]. Both of the enrichments are C_1 continuous inside an enriched element and C_0 continuous over the whole domain. Based on these properties, a regularized Heaviside function [10] and a regularized level set function [17] are used as the enrichments for the translational and the rotational displacements, respectively. Both of the enrichments are regularized by the Hermite function over the HGZ. The HGZ is an area with non-smooth displacement approximation fields. As regularized enrichments are employed in the present work, the strain energy inside a HGZ can be expressed by the derivative of the non-smooth displacement field. It should be noted that the HGZ *should not* be regarded as an exclusive yield line or a yielded area, because there is no technique in the present formulation to prevent a point outside the HGZ from yielding.

Blending elements are major concerns in an XFEM analysis. A blending element is an element in which only part of its nodes are enriched. In blending elements, partition of unity condition cannot be satisfied, which means the enrichment cannot be reproduced. Furthermore, unwanted strain terms occur in blending elements and this may reduce the convergence rate of the XFEM analysis [22]. In order to avoid such problem, shifted enrichment function is adopted, so that the enrichments are only non-zero within the enriched elements [5, 6].

Before the enrichments are formulated, some assumptions on the HGZ are stated as follows:

1) A HGZ is assumed to be a band or a stripe with a constant width along the longitudinal direction of a yield line.
2) The center line of a HGZ is assumed to be perpendicular to the direction of the maximum gradient of the displacement approximation field.
3) The width of a HGZ does not increase during a finite element analysis.
4) An enriched element is cut by *one* HGZ only, which means for each enriched element only a set of enrichment is added into its displacement approximation. However, a node can be enriched by many sets of additional DOF.

In the present formulation, a HGZ is described by a function, $\varphi(\xi, \eta) = 0$, with a parametric width ($\omega \geq 0.0$) as *a priori* information. As shown in Figure 3, an enriched element is divided into two parts: the HGZ and the remaining parts of the element. The parametric width (ω) depends on the size of the enriched element (l_e) and the physical width of the HGZ (l_ns) such that

$$\omega = \frac{l_\mathrm{ns}}{l_\mathrm{e}} \tag{7}$$

The definitions of l_e and l_ns are shown in Figure 3a. An example of the HGZ is shown in Figure 3b, in which the parametric length of the HGZ (ω) is prescribed as 0.4 and the parametric location of it is prescribed as $\varphi = \xi - 0.5 = 0$. A regularized shifted enrichment is constructed over the domain outside the HGZ. A parent coordinate system (ξ^*, η^*) for the HGZ, as shown in Figure 4, is established so that the Hermite functions can be expressed in a consistent way. The Hermite functions (H_t for translation and H_r for rotation) are constructed in the HGZ based on the 4 interpolation points (the four corner point φ_{00}, φ_{10}, φ_{11} and φ_{01} of the HGZ in Figure 3b), 8 tangent vectors (the first partial derivative of the enrichment functions with respect to ξ^* and η^* at the four points) and 4 second derivative vectors (the cross partial derivative of the enrichment functions at the four points). The HGZ parent coordinate system can be established by the following rule:

(i) The point with the smallest value of ξ is chosen as the origin point of the HGZ parent coordinate system.

(ii) If two points share the same smallest value of ξ, the point with a smaller value of η is chosen as the origin.

(iii) The ξ^*-axis points to the adjacent point from the origin and the cosine of the angle between ξ^*-axis and ξ-axis is positive.

(iv) If both of the two adjacent points satisfy rule (iii), the axis with a negative sine of the angle with respect to ξ-axis is chosen as the ξ^*-axis.

(v) Finally, the other edge passing through the origin is the η^*-axis.

The enrichment *S* for the rotation approximation is expressed by

$$S_i(\xi,\eta) = R(\varphi) - H(\varphi_i) = \begin{cases} H_\mathrm{r} - H(\varphi_i) & ;|\varphi| < 0.5\omega \\ H(\varphi) - H(\varphi_i) & ;\text{otherwise} \end{cases} \tag{8}$$

where $R(\varphi)$ is the regularized enrichment for the *rotational displacement* approximation field before shifting, and a plot of *R* for the particular case is shown in Figure 5. $H(\varphi)$ is the Heaviside function and $H(\varphi_i)$ (i = 1, 2, …, 6) is the nodal value of the Heaviside function at node *i*.

$$H(\varphi) = \begin{cases} -1 & \varphi < 0 \\ 0 & \varphi = 0 \\ 1 & \varphi > 0 \end{cases} \tag{9}$$

The regularized shifted enrichment for the *translational displacement* approximation field used in the present formulation is of the form:

$$F(\varphi)=\begin{cases} H_{\mathrm{t}} & |\varphi|<0.5\omega \\ \sum\limits_{k=1}^{6} N_k\,|\varphi_k| - \left|\sum\limits_{k=1}^{6}\varphi_k N_k\right| & \text{otherwise} \end{cases} \tag{10}$$

where N_k are the standard shape functions for a 6-node triangular element. The plot of F for the particular case is shown in Figure 6.

In Equation (8) and Equation (10), the Hermite functions for rotation and translation approximations, H_{r} and H_{t}, are constructed by the matrix expression as:

$$H_{\mathrm{r}} = \mathbf{P}_{\xi*}{}^{\mathrm{T}} \cdot \mathbf{M}^{\mathrm{T}} \cdot \mathbf{G}_{\mathrm{r}} \cdot \mathbf{M} \cdot \mathbf{P}_{\eta*} \tag{11}$$

$$H_{\mathrm{t}} = \mathbf{P}_{\xi*}{}^{\mathrm{T}} \cdot \mathbf{M}^{\mathrm{T}} \cdot \mathbf{G}_{\mathrm{t}} \cdot \mathbf{M} \cdot \mathbf{P}_{\eta*} \tag{12}$$

where $\mathbf{G}_{\mathrm{r}}$ and $\mathbf{G}_{\mathrm{t}}$ are the Hermite geometry vectors for rotational and translational DOFs, respectively. $\mathbf{M}$ is the Hermite matrix. $\mathbf{P}_{\xi*}$ and $\mathbf{P}_{\eta*}$ are the cubic power basis vectors of ξ^* and η^*, respectively.

$$\mathbf{G}_{\mathrm{r}} = \begin{pmatrix} S(\varphi_{00}) & S(\varphi_{01}) & S_{,\eta^*}(\varphi_{00}) & S_{,\eta^*}(\varphi_{01}) \\ S(\varphi_{10}) & S(\varphi_{11}) & S_{,\eta^*}(\varphi_{10}) & S_{,\eta^*}(\varphi_{11}) \\ S_{,\xi^*}(\varphi_{00}) & S_{,\xi^*}(\varphi_{01}) & S_{,\xi^*\eta^*}(\varphi_{00}) & S_{,\xi^*\eta^*}(\varphi_{01}) \\ S_{,\xi^*}(\varphi_{10}) & S_{,\xi^*}(\varphi_{11}) & S_{,\xi^*\eta^*}(\varphi_{10}) & S_{,\xi^*\eta^*}(\varphi_{11}) \end{pmatrix} = \begin{pmatrix} S(\varphi_{00}) & S(\varphi_{01}) & 0 & 0 \\ S(\varphi_{10}) & S(\varphi_{11}) & 0 & 0 \\ 0 & 0 & 0 & 0 \\ 0 & 0 & 0 & 0 \end{pmatrix} \tag{13}$$

$$\mathbf{G}_{\mathrm{t}} = \begin{pmatrix} F(\varphi_{00}) & F(\varphi_{01}) & F_{,\eta^*}(\varphi_{00}) & F_{,\eta^*}(\varphi_{01}) \\ F(\varphi_{10}) & F(\varphi_{11}) & F_{,\eta^*}(\varphi_{10}) & F_{,\eta^*}(\varphi_{11}) \\ F_{,\xi^*}(\varphi_{00}) & F_{,\xi^*}(\varphi_{01}) & F_{,\xi^*\eta^*}(\varphi_{00}) & F_{,\xi^*\eta^*}(\varphi_{01}) \\ F_{,\xi^*}(\varphi_{10}) & F_{,\xi^*}(\varphi_{11}) & F_{,\xi^*\eta^*}(\varphi_{10}) & F_{,\xi^*\eta^*}(\varphi_{11}) \end{pmatrix} \tag{14}$$

$$\mathbf{M} = \begin{bmatrix} 1 & 0 & -3 & 2 \\ 0 & 0 & 3 & -2 \\ 0 & 1 & -2 & 1 \\ 0 & 0 & -1 & 1 \end{bmatrix},\ \mathbf{P}_{\xi} = \begin{pmatrix} 1 & \xi^* & \xi^{*2} & \xi^{*3} \end{pmatrix}^{\mathrm{T}},\ \mathbf{P}_{\eta} = \begin{pmatrix} 1 & \eta^* & \eta^{*2} & \eta^{*3} \end{pmatrix}^{\mathrm{T}} \tag{15}$$

In Equation (13) and Equation (14), $S_{,\xi*}=\partial S/\partial\xi^*$ refers to the partial derivative. It is obvious that $\partial S/\partial\xi^*=\partial S/\partial\eta^*=\partial^2 S/\partial\xi^*\partial\eta^*= 0$ outside the HGZ.

The first derivatives of the enrichment functions S_i and F with respect to the element parent coordinates ξ and η over the HGZ domain are of the form

$$\frac{\partial S_i}{\partial \boldsymbol{\xi}} = \frac{\partial R}{\partial \boldsymbol{\xi}} = H_{\mathrm{r},\boldsymbol{\xi}}, \quad \frac{\partial F}{\partial \boldsymbol{\xi}} = H_{\mathrm{t},\boldsymbol{\xi}} \tag{16}$$

$$H_{\mathrm{r},\boldsymbol{\xi}} = \mathbf{P}_{\xi^*,\boldsymbol{\xi}}{}^{\mathrm{T}} \cdot \mathbf{M}^{\mathrm{T}} \cdot \mathbf{G}_{\mathrm{r}} \cdot \mathbf{M} \cdot \mathbf{P}_{\eta^*} + \mathbf{P}_{\xi^*}{}^{\mathrm{T}} \cdot \mathbf{M}^{\mathrm{T}} \cdot \mathbf{G}_{\mathrm{r}} \cdot \mathbf{M} \cdot \mathbf{P}_{\eta^*,\boldsymbol{\xi}} \tag{17}$$

$$H_{\mathrm{t},\boldsymbol{\xi}} = \mathbf{P}_{\xi^*,\boldsymbol{\xi}}{}^{\mathrm{T}} \cdot \mathbf{M}^{\mathrm{T}} \cdot \mathbf{G}_{\mathrm{t}} \cdot \mathbf{M} \cdot \mathbf{P}_{\eta^*} + \mathbf{P}_{\xi^*}{}^{\mathrm{T}} \cdot \mathbf{M}^{\mathrm{T}} \cdot \mathbf{G}_{\mathrm{t}} \cdot \mathbf{M} \cdot \mathbf{P}_{\eta^*,\boldsymbol{\xi}} \tag{18}$$

and

$$\mathbf{P}_{\xi^*,\boldsymbol{\xi}} = \begin{pmatrix} 0 & 1 & 2\xi^* & 3\xi^{*2} \end{pmatrix}^{\mathrm{T}} \begin{pmatrix} \dfrac{\partial \xi^*}{\partial \xi} & \dfrac{\partial \xi^*}{\partial \eta} \end{pmatrix} \tag{19}$$

$$\mathbf{P}_{\eta^*,\boldsymbol{\xi}} = \begin{pmatrix} 0 & 1 & 2\eta^* & 3\eta^{*2} \end{pmatrix}^{\mathrm{T}} \begin{pmatrix} \dfrac{\partial \eta^*}{\partial \xi} & \dfrac{\partial \eta^*}{\partial \eta} \end{pmatrix} \tag{20}$$

where chain rule is applied and, in Equation (16), $\partial / \partial \boldsymbol{\xi} = (\partial / \partial \xi, \partial / \partial \eta)^{\mathrm{T}}$.

The plots of the first derivatives of the enrichment S and F over the whole element domain for the particular case that $\varphi = \xi - 0.5 = 0$ and $\omega = 0.4$ are shown in Figure 7 to Figure 9.

4 The conventional plate element formulation

4.1 Coordinate systems, element DOF and kinematic equation

A local coordinate system is established for each plate element, which is placed on the global XY plane. The axes of the local coordinate system can be found by the following expression:

$$\mathbf{e}_{\mathrm{x}} = \frac{\mathbf{X}_2 - \mathbf{X}_1}{\left|\mathbf{X}_2 - \mathbf{X}_1\right|}, \quad \mathbf{e}_{\mathrm{z}} = \mathbf{e}_{\mathrm{Z}} = (0,0,1)^{\mathrm{T}}, \quad \mathbf{e}_{\mathrm{y}} = \mathbf{e}_{\mathrm{z}} \times \mathbf{e}_{\mathrm{x}} \tag{21}$$

where $\mathbf{X}_1$ and $\mathbf{X}_2$ are the global coordinates of node 1 and node 2 (Figure 10) of the element, and $\mathbf{e}_Z$ is a unit vector along the global Z-axis.

There are five degrees of freedom (DOF) per node in the present plate element with $\mathbf{u}_i = (u_i, v_i, w_i, \theta_{xi}, \theta_{yi})^T$ in the local coordinate system and $\mathbf{U}_i = (U_i, V_i, W_i, \psi_{xi}, \psi_{yi})^T$ in the global coordinate system (i =1, 2, …, 6). u_i, v_i, U_i and V_i are the in-plane displacements at node i, w_i and W_i are the out-of-plane deflection at node i and θ_{xi}, ψ_{xi} and θ_{yi}, ψ_{yi} are the rotational angle with respect to x-, X- and y-, Y-axis, respectively. In a small-displacement analysis, the relationship between the local and the global nodal displacement can be expressed as

$$\mathbf{u}_i = \mathbf{T}_i \mathbf{U}_i \tag{22}$$

where $\mathbf{T}_i$ is the transformation matrix for the global and the local displacement.

$$\mathbf{T}_i = \begin{bmatrix} \mathbf{R} & \mathbf{0} \\ \mathbf{0} & \mathbf{R}_\theta \end{bmatrix} \tag{23}$$

$\mathbf{R}$ and $\mathbf{R}_\theta$ are the sub-matrix of $\mathbf{T}_i$ corresponding to translational and rotational displacement, respectively. $\mathbf{R}$ and $\mathbf{R}_\theta$ are of the form:

$$\mathbf{R} = \begin{bmatrix} \mathbf{R}_\theta & \mathbf{0} \\ \mathbf{0} & 1 \end{bmatrix}, \ \mathbf{R}_\theta = \begin{bmatrix} \mathbf{e}_{x1} & \mathbf{e}_{y1} \\ \mathbf{e}_{x2} & \mathbf{e}_{y2} \end{bmatrix} \tag{24}$$

where $\mathbf{e}_{x1}$, $\mathbf{e}_{x2}$ are the X- and the Y-component of the unit vector $\mathbf{e}_x$, $\mathbf{e}_{y1}$ and $\mathbf{e}_{y2}$ are the X and the Y-component of the unit vector $\mathbf{e}_y$.

The displacement field, $\mathbf{u} = (u, v, w, \theta_x, \theta_y)^T$, can be expressed as

$$\mathbf{u} = \sum_{i=1}^{6} N_i \mathbf{u}_i \tag{25}$$

where N_i (i =1, 2, …, 6) are the standard isoparametric shape functions for a six-node triangular plate element.

A layered model, as shown in Figure 11 with equal thickness for each layer is used in the present plate element. The normal strain varies along the thickness direction and the shear strain is assumed to be constant along the thickness direction. The membrane strain ε_{m}, bending strain in the j^{th} layer $\varepsilon_{\mathrm{b}j}$ and the shear strain γ can be expressed by

$$\varepsilon_{\mathrm{m}}=\begin{Bmatrix}\dfrac{\partial u}{\partial x}\\ \dfrac{\partial v}{\partial y}\\ \dfrac{\partial u}{\partial y}+\dfrac{\partial v}{\partial x}\end{Bmatrix},\quad \boldsymbol{\varepsilon}_{\mathrm{b}j}=-z_j\boldsymbol{\chi}=-z_j\begin{Bmatrix}\dfrac{\partial \beta_x}{\partial x}\\ \dfrac{\partial \beta_y}{\partial y}\\ \dfrac{\partial \beta_y}{\partial x}+\dfrac{\partial \beta_x}{\partial y}\end{Bmatrix},\quad \boldsymbol{\gamma}=\begin{Bmatrix}-\beta_x+\dfrac{\partial w}{\partial x}\\ -\beta_y+\dfrac{\partial w}{\partial y}\end{Bmatrix} \tag{26}$$

where z_j is the distance between the middle surface of the j^{th} layer and the reference surface; $\boldsymbol{\chi}$ is the curvature, β_{x} and β_{y} are the rotation angles of the lines normal to the undeformed neutral surface in *x-z* and *y-z* plane, respectively, which can be written in matrix form as [23]

$$\begin{pmatrix}\beta_{\mathrm{x}}\\ \beta_{\mathrm{y}}\end{pmatrix}=\begin{bmatrix}0 & -1\\ 1 & 0\end{bmatrix}\begin{pmatrix}\theta_{\mathrm{x}}\\ \theta_{\mathrm{y}}\end{pmatrix},\ \text{or}\ \boldsymbol{\beta}=\mathbf{R}_{\beta}\boldsymbol{\theta} \tag{27}$$

4.2 The discrete shear gap method (DSG)

Shear locking is one of the major concerns in a compatible plate element formulation. The compatible strain field introduces additional energy into the element, and the plate element behaves much stiffer than expected for a thin plate. Several methods [24-27] have been proposed to circumvent shear locking in a triangular element. In the present element, the DSG method [24] is employed.

In the DSG method, the shear strain field is assumed as

$$\tilde{\gamma}_{\xi\zeta}=\frac{\partial \Delta w_{\xi\zeta}}{\partial \xi},\quad \tilde{\gamma}_{\eta\zeta}=\frac{\partial \Delta w_{\eta\zeta}}{\partial \eta} \tag{28}$$

where $\Delta w_{\xi\zeta}$ is the shear gap obtained by integration of the compatible shear strain terms.

$$\Delta w_{\xi\zeta} = \sum_{i=1}^{6} N_i \Delta w_{\xi\zeta i} = \sum_{i=1}^{6} N_i \int_{\xi_1}^{\xi_i} \gamma_{\xi\zeta} \mathrm{d}\xi , \quad \Delta w_{\eta\zeta} = \sum_{i=1}^{6} N_i \Delta w_{\eta\zeta i} = \sum_{i=1}^{6} N_i \int_{\eta_1}^{\eta_i} \gamma_{\eta\zeta} \mathrm{d}\eta \qquad (29)$$

where $\gamma_{\xi\zeta}$ and $\gamma_{\eta\zeta}$ are compatible shear strain in curvilinear coordinate system.

Substituting Equation (29) into Equation (28), the assumed shear strain can be expressed as

$$\gamma_{\xi\zeta} = -\sum_{i=1}^{6} h_{\xi i} \beta_{\xi i} + \sum_{i=1}^{6} \frac{\partial N_i}{\partial \xi} w_i \qquad (30)$$

$$\gamma_{\eta\zeta} = -\sum_{i=1}^{6} h_{\eta i} \beta_{\eta i} + \sum_{i=1}^{6} \frac{\partial N_i}{\partial \eta} w_i \qquad (31)$$

where $h_{\xi i}$ and $h_{\eta i}$ are the assumed shear strain interpolation functions for the rotation angle β_ξ and β_η in the curvilinear coordinate system, and they can be expressed explicitly as:

$$h_{\xi 1} = -\xi + 4\xi\eta + \frac{2}{3} - 3\eta , \; h_{\xi 2} = \xi - \frac{1}{3} , \; h_{\xi 3} = -\eta , \; h_{\xi 4} = -4\xi\eta + \frac{2}{3} , \; h_{\xi 5} = 4\xi\eta , \; h_{\xi 6} = -4\xi\eta + 4\eta \qquad (32)$$

$$h_{\eta 1} = -\eta + 4\xi\eta + \frac{2}{3} - 3\xi , \; h_{\eta 2} = -\xi , \; h_{\eta 3} = \eta - \frac{1}{3} , \; h_{\eta 4} = -4\xi\eta + 4\xi , \; h_{\eta 5} = 4\xi\eta , \; h_{\eta 6} = -4\xi\eta + \frac{2}{3} \qquad (33)$$

4.3 The stiffness matrix and the internal force vector

The element stiffness matrix $\mathbf{K}_\mathrm{e}$ and the element internal force vector $\mathbf{f}_\mathrm{e}$ can be expressed as

$$\mathbf{K}_\mathrm{e} = \mathbf{T}^\mathrm{T} \mathbf{K}_\mathrm{l} \mathbf{T} , \quad \mathbf{f}_\mathrm{e} = \mathbf{T}^\mathrm{T} \mathbf{f}_\mathrm{l} \qquad (34)$$

$$\mathbf{T} = \begin{bmatrix} \mathbf{T}_1 & & & \\ & \mathbf{T}_2 & & \\ & & \ddots & \\ & & & \mathbf{T}_6 \end{bmatrix} \qquad (35)$$

$\mathbf{K}_\mathrm{l}$ and $\mathbf{f}_\mathrm{l}$ are the stiffness matrix and the internal force vector in the local coordinate system.

$$\mathbf{K}_\mathrm{l} = t\int \tilde{\mathbf{B}}_\mathrm{s}{}^\mathrm{T}\mathbf{D}\tilde{\mathbf{B}}_\mathrm{s}\mathrm{d}A + \sum_{j=1}^{nlayer} t_j \int \left(\mathbf{B}_\mathrm{m} - z_j\mathbf{B}_\chi\right)^\mathrm{T} \mathbf{D}_j \left(\mathbf{B}_\mathrm{m} - z_j\mathbf{B}_\chi\right)\mathrm{d}A \tag{36}$$

$$\mathbf{f}_\mathrm{l} = t\int \tilde{\mathbf{B}}_\mathrm{s}{}^\mathrm{T}\boldsymbol{\tau}\mathrm{d}A + \sum_{j=1}^{nlayer} t_j \int \left(\mathbf{B}_\mathrm{m} + z_j\mathbf{B}_\chi\right)^\mathrm{T} \boldsymbol{\sigma}_j\mathrm{d}A \tag{37}$$

where t is the total thickness of the element. $\tilde{\mathbf{B}}_\mathrm{s}$ is the strain-displacement matrix for the assumed shear strain. t_j is the thickness of the j^th layer of a plate element. $\mathbf{B}_\chi$ is the strain-displacement matrix for the compatible bending strain. $\mathbf{B}_\mathrm{m}$ is the strain-displacement matrix for the compatible membrane strain. $\mathbf{D}$ is the material matrix and $\mathbf{D}_j$ is the material matrix for plane-stress cases of the j^th layer.

4.4 The elasto-plastic model

In the present plate element, the out-of-plane stress components are not taken into account in the formulation [28]. The exclusion of the out-of-plane stress components is acceptable, since in membrane-dominant cases, the transverse shear stresses are relatively small and can be omitted. On the other hand, in bending-dominant cases, the transverse shear stresses are assumed as uniformly distributed along the thickness direction. However, as it is well known that the transverse stress is zero at the extreme fibres and maximum at the mid-surface which will be yielded at the very late stage, initial yielding is not affected by this omission.

Hence, the J_2 yield criteria for plane stress cases can be simplified as:

$$f\left(\sigma_\mathrm{x}, \sigma_\mathrm{y}, \tau_\mathrm{xy}\right) = \left[\sigma_\mathrm{x}^2 + \sigma_\mathrm{y}^2 - \sigma_\mathrm{x}\sigma_\mathrm{y} + 3\tau_\mathrm{xy}^2\right]^{1/2} - \sigma_0 = \sigma_\mathrm{e} - \sigma_0 \tag{38}$$

where σ_e is the effective stress, and σ_0 is the yield strength.

According to the Prandtl-Reuss flow rule [29], the plastic part for incremental strain is:

$$\mathrm{d}\boldsymbol{\varepsilon}_{\mathrm{p}} = \left(\mathrm{d}\varepsilon_{\mathrm{px}} \quad \mathrm{d}\varepsilon_{\mathrm{py}} \quad \mathrm{d}\varepsilon_{\mathrm{pxy}}\right)^{\mathrm{T}} = \mathrm{d}\lambda\mathbf{a} \tag{39}$$

where dλ is plastic strain rate multiplier and **a** is flow vector which can be expressed as:

$$\mathbf{a} = \frac{\partial f}{\partial \boldsymbol{\sigma}^{\mathrm{T}}} = \left(\frac{\partial f}{\partial \sigma_{\mathrm{x}}} \quad \frac{\partial f}{\partial \sigma_{\mathrm{y}}} \quad \frac{\partial f}{\partial \tau_{\mathrm{xy}}}\right)^{\mathrm{T}} \tag{40}$$

In the present element, as plane-stress J_2 flow theory is employed, the incremental plastic strain can be expressed further as:

$$\mathrm{d}\boldsymbol{\varepsilon}_{\mathrm{p}} = \mathrm{d}\lambda\mathbf{P}\boldsymbol{\sigma} \tag{41}$$

Where the matrix P and the vector σ are of the form:

$$\mathbf{P} = \frac{1}{3}\begin{bmatrix} 2 & -1 & 0 \\ -1 & 2 & 0 \\ 0 & 0 & 6 \end{bmatrix}, \qquad \boldsymbol{\sigma} = \begin{pmatrix} \sigma_{\mathrm{x}} \\ \sigma_{\mathrm{y}} \\ \tau_{\mathrm{xy}} \end{pmatrix} \tag{42}$$

As shown in Figure 12, the stress can be updated by [29]

$$\boldsymbol{\sigma}_{\mathrm{C}} = \mathbf{D}\left(\boldsymbol{\varepsilon}_{\mathrm{C}} - \boldsymbol{\varepsilon}_{\mathrm{pC}}\right) = \mathbf{D}\left(\boldsymbol{\varepsilon}_{\mathrm{C}} - \boldsymbol{\varepsilon}_{\mathrm{pA}} - \mathrm{d}\boldsymbol{\varepsilon}_{\mathrm{p}}\right) = \boldsymbol{\sigma}_{\mathrm{B}} - \mathrm{d}\lambda\mathbf{D}\mathbf{a}_{\mathrm{C}} \tag{43}$$

where $\boldsymbol{\sigma}_{\mathrm{C}}$ is the desired stress, $\boldsymbol{\sigma}_{\mathrm{A}}$ is the stress state of the starting point of the current incremental step, $\boldsymbol{\sigma}_{\mathrm{B}}$ is the trial stress in which the incremental strain of the current step is assumed as elastic and $\mathrm{d}\boldsymbol{\varepsilon}_{\mathrm{p}} = \boldsymbol{\varepsilon}_{\mathrm{pC}} - \boldsymbol{\varepsilon}_{\mathrm{pA}}$ is the incremental plastic strain for the current step.

Substituting Equation (40) into Equation (43), the desired stress state $\boldsymbol{\sigma}_{\mathrm{C}}$ can be expressed as [30]

$$\boldsymbol{\sigma}_{\mathrm{C}} = \boldsymbol{\Xi}\mathbf{D}\boldsymbol{\sigma}_{\mathrm{B}} \tag{44}$$

$$\boldsymbol{\Xi} = \left(\mathbf{D}^{-1} + \mathrm{d}\lambda\mathbf{P}\right)^{-1} \tag{45}$$

where **I** is three-order unit matrix. Equation (44) established an expression of $\boldsymbol{\sigma}_{\mathrm{C}}$ in which the plastic multiplier dλ is the only unknown. The plastic multiplier dλ can be obtained through a backward-Euler algorithm by solving a nonlinear equation whose physical meaning is the satisfactory of the yield criteria at the stress state C:

$$f\left(\boldsymbol{\sigma}_{\mathrm{C}}\right)=f\left(\mathrm{d}\lambda\right)=0 \tag{46}$$

5 The enriched plate element formulation

The local coordinate system of an enriched element is established in the same way as an unenriched element, (Equation (21)). There are eight DOFs per node in enriched elements, which is $\mathbf{u}_{\mathrm{enr}i} = (u_i, v_i, w_i, \theta_{\mathrm{x}i}, \theta_{\mathrm{y}i}, a_{\mathrm{x}i}, a_{\mathrm{y}i}, b_i)^{\mathrm{T}}$ in the local coordinate system and $\mathbf{U}_{\mathrm{enr}i} = (U_i, V_i, W_i, \psi_{\mathrm{x}i}, \psi_{\mathrm{y}i}, A_{\mathrm{x}i}, A_{\mathrm{y}i}, B_i)^{\mathrm{T}}$ in the global coordinate system. The variables $a_{\mathrm{x}i}$ and $a_{\mathrm{y}i}$ are the additional rotational DOF with respective to the x- and y-axis whereas b_i is the additional translational DOF in the local coordinate system. The variables $A_{\mathrm{x}i}$ and $A_{\mathrm{y}i}$ are the additional rotational DOF with respect to X- and Y-axis while B_i is the additional translational DOF in the global coordinate system. The relationship between the local and the global nodal displacement can be expressed as

$$\mathbf{u}_{\mathrm{enr}i}=\mathbf{T}_{\mathrm{enr}i}\mathbf{U}_{\mathrm{enr}i} \tag{47}$$

where $\mathbf{T}_{\mathrm{enr}i}$ is the transformation matrix for a node in an enriched element.

$$\mathbf{T}_{\mathrm{enr}i}=\begin{bmatrix} \mathbf{R} & \mathbf{0} & \mathbf{0} & \mathbf{0} \\ \mathbf{0} & \mathbf{R}_\theta & \mathbf{0} & \mathbf{0} \\ \mathbf{0} & \mathbf{0} & \mathbf{R}_\theta & \mathbf{0} \\ \mathbf{0} & \mathbf{0} & \mathbf{0} & 1 \end{bmatrix} \tag{48}$$

The displacement field can be approximated by the sum of the smooth part and the non-smooth part:

$$w_{\mathrm{h}}=w+b=\sum_{i=1}^{6}N_i w_i+\sum_{i=1}^{6}L_i b_i \tag{49}$$

$$\theta_{\mathrm{xh}}=\theta_{\mathrm{x}}+a_{\mathrm{x}}=\sum_{i=1}^{6}N_i\theta_{\mathrm{x}i}+\sum_{i=1}^{6}M_i a_{\mathrm{x}i} \tag{50}$$

$$\theta_{\mathrm{yh}} = \theta_{\mathrm{y}} + a_{\mathrm{y}} = \sum_{i=1}^{6} N_i \theta_{\mathrm{y}i} + \sum_{i=1}^{6} M_i a_{\mathrm{y}i} \tag{51}$$

where a_{x}, a_{y} and b are the non-smooth displacement approximation fields for rotations and translations, L_i and M_i are the interpolation functions for the non-smooth translation and rotation displacement, respectively. It should be noted that in a small deformation analysis, the rotational DOF can be regarded as a vector as the translational DOF [31] so that Equation (51) is valid. L_i and M_i can be found by the multiplication of the non-smooth enrichment and window functions. In the present XFEM formulation, the standard shape functions for a 6-node triangular element are used as window functions for the localization of the enrichments:

$$M_i = N_i S_i \tag{52}$$

$$L_i = N_i F \tag{53}$$

where S_i and F are enrichments for rotational and translational displacement, respectively, (Equation (8) and Equation (10)).

The bending strain $\varepsilon_{\mathrm{benr}}$ and the shear strain γ_{enr} at an arbitrary point in an enriched element can be expressed by

$$\boldsymbol{\varepsilon}_{\mathrm{benr}} = -z\boldsymbol{\chi}_{\mathrm{enr}} = -z \begin{pmatrix} \dfrac{\partial \beta_{\mathrm{x}}}{\partial x} + \dfrac{\partial \alpha_{\mathrm{x}}}{\partial x} \\ \dfrac{\partial \beta_{\mathrm{y}}}{\partial y} + \dfrac{\partial \alpha_{\mathrm{y}}}{\partial y} \\ \dfrac{\partial \beta_{\mathrm{y}}}{\partial x} + \dfrac{\partial \alpha_{\mathrm{y}}}{\partial x} + \dfrac{\partial \beta_{\mathrm{x}}}{\partial y} + \dfrac{\partial \alpha_{\mathrm{x}}}{\partial y} \end{pmatrix}, \quad \boldsymbol{\gamma}_{\mathrm{enr}} = \begin{pmatrix} -\beta_{\mathrm{x}} - \alpha_{\mathrm{x}} + \dfrac{\partial w}{\partial x} + \dfrac{\partial b}{\partial x} \\ -\beta_{\mathrm{y}} - \alpha_{\mathrm{y}} + \dfrac{\partial w}{\partial y} + \dfrac{\partial b}{\partial y} \end{pmatrix} \tag{54}$$

where α_{x} and α_{y} are the rotation angles of the lines normal to the undeformed neutral surface in x-z and y-z plane due to the non-smooth rotation:

$$\begin{pmatrix} \alpha_{\mathrm{x}} \\ \alpha_{\mathrm{y}} \end{pmatrix} = \begin{bmatrix} 0 & -1 \\ 1 & 0 \end{bmatrix} \begin{pmatrix} a_{\mathrm{x}} \\ a_{\mathrm{y}} \end{pmatrix} \tag{55}$$

It should be noted that the membrane strain is not enriched in the present formulation.

The stiffness matrix $\mathbf{K}_{\mathrm{eenr}}$ and the internal force vector $\mathbf{f}_{\mathrm{eenr}}$ of an enriched element can be expressed as

$$\mathbf{K}_{\mathrm{eenr}} = \mathbf{T}_{\mathrm{enr}}{}^{\mathrm{T}} \mathbf{K}_{\mathrm{lenr}} \mathbf{T}_{\mathrm{enr}}, \quad \mathbf{f}_{\mathrm{eenr}} = \mathbf{T}_{\mathrm{enr}}{}^{\mathrm{T}} \mathbf{f}_{\mathrm{lenr}} \tag{56}$$

$$\mathbf{T}_{\mathrm{enr}} = \begin{bmatrix} \mathbf{T}_{\mathrm{enr1}} & & & \\ & \mathbf{T}_{\mathrm{enr2}} & & \\ & & \ddots & \\ & & & \mathbf{T}_{\mathrm{enr6}} \end{bmatrix} \tag{57}$$

In Equation (56), $\mathbf{K}_{\mathrm{lenr}}$ and $\mathbf{f}_{\mathrm{lenr}}$ are the stiffness matrix and the internal force vector of an enriched element in the local coordinate system.

$$\begin{aligned} \mathbf{K}_{\mathrm{lenr}} &= t\int \left(\tilde{\mathbf{B}}_{\mathrm{s}} + \mathbf{B}_{\mathrm{b}} + \mathbf{B}_{\alpha}\right)^{\mathrm{T}} \mathbf{D}\left(\tilde{\mathbf{B}}_{\mathrm{s}} + \mathbf{B}_{\mathrm{b}} + \mathbf{B}_{\alpha}\right) \mathrm{d}A \\ &+ \sum_{j=1}^{nlayer} t_j \int \left(\mathbf{B}_{\mathrm{m}} - z_j \mathbf{B}_{\chi} - z_j \mathbf{B}_{\alpha}\right)^{\mathrm{T}} \mathbf{D}_j \left(\mathbf{B}_{\mathrm{m}} - z_j \mathbf{B}_{\chi} - z_j \mathbf{B}_{\alpha}\right) \mathrm{d}A \end{aligned} \tag{58}$$

$$\mathbf{f}_{\mathrm{lenr}} = t\int \left(\tilde{\mathbf{B}}_{\mathrm{s}} + \mathbf{B}_{\mathrm{A}}\right)^{\mathrm{T}} \boldsymbol{\tau} \mathrm{d}A + \sum_{j=1}^{nlayer} t_j \int \left(\mathbf{B}_{\mathrm{m}} - z_j \mathbf{B}_{\chi} - z_j \mathbf{B}_{\mathrm{B}}\right)^{\mathrm{T}} \boldsymbol{\sigma}_j \mathrm{d}A \tag{59}$$

where $\mathbf{B}_{\alpha}$ is the strain-displacement matrix for additional rotational DOF, and $\mathbf{B}_{\mathrm{b}}$ is the strain-displacement matrix for additional translational DOF. It is obvious that the stiffness matrix for an enriched element is still symmetric.

6 The implementation of the XFEM formulation

6.1 Partition of an enriched element

An enriched element is partitioned by a HGZ to a maximum of 3 sub-domains. The number of sub-domains depends on the way the HGZ cuts across an element. Several cases can be categorized as shown in Figure 13, in which ‘QU’ refers to a quadrilateral area, ‘TR’ refers to a triangular area, ‘nH’ refers to the area outside the HGZ and ‘H’ refers to a HGZ.

In Figure 13(a), the enriched element is partitioned into one quadrilateral non-smooth sub-domain, one quadrilateral smooth sub-domain and one triangular smooth sub-domain. In Figure 13(b), one triangular non-smooth sub-domain and one quadrilateral smooth sub-domain are generated. In Figure 13(c), one quadrilateral non-smooth sub-domain and one triangular smooth sub-domain are generated. In Figure 13(d), two triangular smooth sub-domains and one pentagon non-smooth sub-domain are generated. In Figure 13(d), the pentagon HGZ is further divided into two quadrilateral sub-domains where numerical integration is conducted.

The partition of an enriched element is conducted in the initial stage of a numerical analysis and the enrichment is added into the formulation at the beginning of an analysis, therefore it is unnecessary to determine when to introduce the enrichment into an analysis.

6.2 Shear locking and numerical integration scheme

From numerical point of view, shear locking could be a major concern in the present XFEM formulation. Although shear locking is controlled by the DSG method for the smooth part, it is not easy to apply the existing assumed strain method to the XFEM formulation. In the assumed strain methods, an assumed strain field, instead of the compatible strain field, is used over the whole domain of an element. The assumed strain and the compatible strain are equal at some selected points, known as optimal points [32]. However, in XFEM formulation, it is difficult to propose a consistent way to assume a good strain field because the non-smoothness does not pass an enriched element in a unique way and there could be several possibilities of partition of an enriched element. On the other hand, the ‘optimal’ strain points in a normal element may not be so optimal in an enriched element.

Nevertheless, reduced integration could be a choice to control shear locking. If the in-plane variation of the tangential modulus of the material is not taken into account, the 6 × 6 Gaussian integration scheme is regarding as the full integration scheme for the present XFEM element. However, shear locking occurs if full integration scheme is used. Hence, in the present XFEM element, the 4 × 4 Gaussian integration scheme is employed in each sub-domain. While in some special cases listed in Appendix A and Appendix B, the 3 × 3 Gaussian integration scheme can be used in each sub-domain.

It is shown in Figure 13 that an enriched element is at least divided into two sub-domains. Hence, a 3 × 3 Gaussian integration scheme in both sub-domains provides 18 integration points (5 × 18 = 90 constraints) for the element. On the other hand, in the present XFEM formulation, the translational DOF u and v are decoupled from the other DOF, so (8 – 2) × 6 = 36 constraints are required to avoid matrix singularity due to numerical integration [33].

7 Numerical Examples

7.1 Example 1: A flat strip with two fully fixed ends

A flat rectangular plate is tested in this example, as shown in Figure 14. The length of the plate is $L = 5.0$ and the width is $b = 1.0$. The plate is fully fixed on the two short edges and free on the two long edges. The Young's modulus is $E = 1 \times 10^6$, while the Poisson's ratio is $\upsilon = 0.0$. The mesh scheme and the location of the three possible HGZ are shown in Figure 15. As the layered model is used in the present XFEM formulation, 5 layers are used for each element in this example.

7.1.1 Study on shear locking and reduced integration

The effect of reduced integration is studied in this example with five cases of different thickness. The yield strength σ_y and the reference loading q_0 is normalized according to the plate thickness (Table 1) so that for all the five cases, the upper bound theoretical failure load factor λ_u obtained from the yield line pattern analysis [25] is all equal to 0.625. The results are shown in Figure 16 and Figure 17 with the results from conventional plate FE analysis with fine mesh (10 × 50 × 2 = 1000 elements) and coarse mesh (1 × 5 × 2 = 10 elements). The parametric width is set as $\omega_1 = \omega_2 = \omega_3 = 0.5$.

It can be seen from Figure 16 that when full integration scheme is used, shear locking occurs. However, as shown in Figure 17, when the reduced integration scheme is used, shear locking is largely alleviated.

7.1.2 Study on the width of the HGZ

In this study, the material and geometric properties of Case 2 in Section 6.1.1 is used. The width of the HGZ (ω) (Equation (7)) varies. The deflection of point A is investigated and the equilibrium paths obtained are shown in Figure 18. The results from XFEM formulation are compared with the result from conventional FEM using a fine mesh (10 × 50 × 2 = 1000 elements) and a coarse mesh (1 × 5 × 2 = 10 elements).

First the width of the middle HGZ (ω_2) is studied. The width of the two side-HGZs is fixed as $\omega_1 = \omega_3 = 0.5$. The width of the middle HGZ (ω_2) varies from 0.3 to 0.9. As shown in Figure 18 it can be seen that in this example the value of ω_2 influences on the prediction ultimate loading a lot. With a greater value of ω_2, a lower prediction of the ultimate loading level will be obtained.

Secondly, the influence from the width of the two side HGZs (ω_1, ω_3) is studied. The width of the two side-HGZs varies from 0.1 to 0.9, while the width of the middle HGZ is fixed as $\omega_2 = 0.5$. It can be seen from Figure 19 that the result from the case $\omega_1 = \omega_3 = 0.1$ gives a better prediction than the other results and the smaller the width of side-HGZ is assumed, the closer the result is to that from conventional finite elements in a fine mesh.

7.1.3 Study on the mesh refinement

In this study, a comparison of the numerical results obtained from different element sizes but with the same l_{ns} is given. Two uniform meshes (mesh 1: 1 × 5 × 2 elements and mesh 2: 2 × 10 × 2 elements) with different element size as shown in Figure 20 are tested. The physical widths of the three yield lines (l_{ns1}=0.45, l_{ns2}=0.5 and l_{ns3}=0.45) are the same in both meshes. It should be noted that in order to avoid the numerical singularity [17] when all elements connected the two fixed ends are wholly occupied by the two HGZs near the fixed ends, the physical length of the two HGZs near the fixed ends ($l_{ns1} = l_{ns3}$ = 0.45) are set slightly smaller than the centre HGZ (l_{ns2} = 0.5).

The results obtained from mesh 1 and mesh 2 with the XFEM analysis and the standard FEM analysis are shown in Figure 21. It can be seen that a refined mesh with the same physical width of HGZ as the coarse mesh provided a better prediction on the ultimate loading level in this example.

A further refined mesh with the XFEM analysis is not tested. It is because the main purpose of the present work is to develop a new XFEM formulation which could give a accurate prediction on the ultimate loading level by using a coarse mesh with only a few elements. A highly refined mesh with XFEM element with size equal to or small than the HGZ shall defect the original target of the present work. Furthermore, the XFEM formulation presented here is supposed to capture a locally non-smooth behavior of a plate, while a non-smoothness region could no longer be considered as local if the element size is reduced in such a way that the HGZ occupies or even larger that an element.

7.2 Example 2: An L-shaped plate with two fully fixed ends

An L-shaped flat plate is tested in this example, as shown in Figure 19. The plate is fully fixed on the two short edges. The geometrical property is shown in Figure 22. The plate thickness is $t = 0.15$. The Young's modulus is $E = 1.0 \times 10^6$, while the Poisson's ratio is $\upsilon = 0.3$. The yield strength is $\sigma_y = 1.0$. The reference load is $q_0 = -3 \times 10^{-3}$. The mesh scheme and the locations of three possible HGZs are shown in Figure 23. It can be seen that in this example, yield zone 3 cuts across the edges of element 5 and element 6 (in Figure 23). It should be noted that in the present XFEM formulation, the enrichments are constructed at the element level by the standard shape functions for the isoparametic 6-node triangular element and the distant-function, therefore the enrichment for yield zone 3 is only C_0 continuous along the common edge of element 5 and element 6. As a layered model is employed in the present formulation, 5 layers are used for each element.

Firstly, the width of the middle HGZ is fixed as l_{ns2} =1.0 and the width of the two side-HGZs ($l_{ns1} = l_{ns3}$) varies from 0.1 to 0.5. The deflection of point A is investigated. The result from XFEM formulation is shown in Figure 24, compared with the result from standard FEM with coarse mesh (as shown in Figure 23), fine mesh (1000 elements) and the result from ANSYS (800 SHELL93 elements [34]) with 5 layers for each element, are used. It can be seen from Figure 24 that a smaller value of l_{ns1} and l_{ns3} provides a lower prediction on the ultimate loading level.

The influence from the width of the middle HGZ is studied. The width of the two side-HGZs is fixed as $l_{ns1} = l_{ns3}$ =0.1 and the width of the middle HGZ varies from 0.6 to 1.2. The result is shown in Figure 25. It can be seen that the predicted ultimate loading level decreases with the assumed value on l_{ns2} increases.

7.3 Example 3: A square plate with roller supports at the four edges

A square plate supported by rollers on the four edges is tested in this example, as shown in Figure 26. The length of edge is 32. The thickness is $t = 1.0$. The Young's modulus is $E = 1.0 \times 10^{10}$, while the Poisson's ratio is $\upsilon = 0.2$. The yield strength is $\sigma_y = 1.0 \times 10^5$. A UDL is applied on the plate with the reference loading $q_0 = 1.0 \times 10^4$. A total of 5 layers are used in each element for the analyses. A quarter of the entire plate is modelled because of the symmetry condition. The yield line is along the diagonal line of the plate. It is shown in Figure 27 that the enrichment for the deflection (F) is C_0 continuous in the direction normal to the yield line. In this example two mesh patterns are tested. In each mesh pattern, four different sizes of the yield line are assumed ($l_{ns1} = 3.2$, $l_{ns2} = 4.8$, $l_{ns3} = 6.4$ and $l_{ns4} = 9.6$). The deflection of the centre point (point A in Figure 26) is investigated.

The results from mesh 1 and mesh 2 with the result from standard FEM with coarse mesh ($2 \times 2 \times 2 = 8$ elements), fine mesh ($20 \times 20 \times 2 = 800$ elements) and the result from yield line pattern analysis [35], which gives $\lambda_u = 0.0586$, are shown in Figure 28 and Figure 29, respectively. In both of the mesh patterns, the greater value of l_{ns} provides a lower ultimate loading level.

8 Conclusions and discussions

An isoparametric plate element with XFEM formulation to model the non-smooth displacement field, resulted from yield lines, is presented in this paper. Regularized shifted enrichments are employed to enrich the deflection and the rotation approximation field to model the non-smoothness in an element. The regularized enrichment provides a natural way to express a discontinuity with finite length which cannot be ignored. The shifted enrichment brings several advantages comparing with the original XFEM formulation: first, the PU condition can be satisfied over the whole physical domain without any other technique. Secondly, there is no unwanted strain term in blending elements. Thirdly, the Kronecker-δ condition can be satisfied on each node in the whole physical domain, thus essential boundary condition can be applied easily.

In a high gradient zone, the Hermite function is adopted as enrichment for both the rotational and the translational approximation fields. As a Hermite function is a polynomial function, a standard Gaussian integration scheme can be used to obtain the stiffness matrix and internal force vector. Since a Hermite function is C_1 continuous over its domain of definition, the high gradient zone is connected with the other part smoothly and the strain field is continuous inside an enriched element. However, it is premature to conclude that the Hermite function is the best selection to enrich the displacement over HGZ for plate structures with different types of boundary and loading conditions. Hence, further study is required to optimize the selection of the enrichment. Besides, shear locking is still a concern for an XFEM plate element. Although the present XFEM plate element with reduced integration provides a more satisfactory result, the stability and the convergence of the reduced integration scheme needs a more rigorous mathematical proof. Therefore, the control of shear locking is a research topic for future studies.

Appendix A: Convergence rate for the non-HGZ

In this section, a proof on the convergence rate of reduced integration scheme for non-HGZ is provided. Assuming that all the edges of the enriched element are straight and the mid-nodes are at the middle of the edges, the location of the HGZ can be expressed as a line on element level in the parent coordinate system:

$$\varphi = a\xi + b\eta + c = 0 \tag{A.1}$$

in which it is assumed that the coefficient b is always non-negative, if b = 0.0, the coefficient a is positive and the coefficient a and b are normalized so that $a^2 + b^2 = 1$

The enrichment for the translational displacement field outside the HGZ part is expressed as:

$$F = \sum_{k=1}^{6} N_k \left|\varphi_k\right| - \left|\sum_{k=1}^{6} \varphi_k N_k\right| = \sum_{k=1}^{6} N_k \left|\varphi_k\right| - \left|a\xi + b\eta + c\right| \tag{A.2}$$

where φ_k is the nodal value of the function φ:

$$\varphi_1 = c,\ \varphi_2 = a + c,\ \varphi_3 = b + c$$

$$\varphi_4 = 0.5a + c,\ \varphi_5 = 0.5a + 0.5b + c,\ \varphi_6 = 0.5b + c \tag{A.3}$$

The expression of the first term in Equation A1 depends on the cases that the line passes through the element.

The perimeter of the triangle element is divided into 6 segments: s1, s2, s3, s4, s5 and s6, as shown in Figure A1. There are 12 cases for this line passing though the element, which are s1s3, s1s4, s1s5, s1s6, s2s3, s2s4, s2s5, s2s6, s3s5, s3s6, s4s5 and s4s6. The notation ‘s1s3’ refers to the case when the center line of the HGZ cutting through the segments s1 and s3 and so on. The polynomial terms appeared and the complete polynomial order of the enrichment function F together with the corresponding minimal integration scheme needed to guarantee the convergence of the non-HGZ in each case are shown in Table A1.

The enrichment S for rotational displacement field outside the HGZ is a constant, therefore the degree of complete polynomial of S is 0. Hence, finally It can be concluded that the 3 × 3 Gaussian integration scheme in non-Hermitian area is acceptable for the cases in which the centre line of HGZ passes through the hypotenuse of the triangle element, and the 4 × 4 Gaussian integration scheme in non-Hermitian area is acceptable for the cases in which the centre line of HGZ passes through the two catheti of the element.

Appendix B: Convergence rate for the HGZ

In this section, a proof on the convergence rate of the reduced integration adopted over HGZ in the present formulation is provided. For general cases, a 4 × 4 Gaussian integration is used over HGZ. However, it is found that in the following four special cases, a 3 × 3 Gaussian integration scheme could be used over the HGZ.

Case 1: the yield line is parallel to one of the catheti of the triangular element in the parent coordinate system (Figure 2b)

Assume that the yield line is parallel to the η – axis and the location of the yield line can be expressed as

$$\varphi = \xi - c = 0 \tag{B.1}$$

Therefore, the enrichment for the non-Hermitian area is written as

$$F = \sum_{k=1}^{6} N_k \left|\varphi_k\right| - \left|\sum_{k=1}^{6} \varphi_k N_k\right| = c\left(1-2\xi\right) + \left(\xi - 2\xi^2\right) + 4\left|0.5-c\right|\left(\xi-\xi^2\right) - \left|\xi - c\right| \tag{B.2}$$

The enrichment is independent of the variable η, so

$$F\left(\varphi_{00}\right) = F\left(\varphi_{01}\right), \quad F\left(\varphi_{10}\right) = F\left(\varphi_{11}\right), \quad \frac{\partial F}{\partial \eta} = 0 \tag{B.3}$$

According to the definition of the ξ^*–η^* coordinate system, $\partial\xi/\partial\eta^* = 0$. Hence,

$$\begin{Bmatrix} \dfrac{\partial F}{\partial \xi^*} \\ \dfrac{\partial F}{\partial \eta^*} \end{Bmatrix} = \begin{bmatrix} \dfrac{\partial \xi}{\partial \xi^*} & \dfrac{\partial \eta}{\partial \xi^*} \\ \dfrac{\partial \xi}{\partial \eta^*} & \dfrac{\partial \eta}{\partial \eta^*} \end{bmatrix} \begin{Bmatrix} \dfrac{\partial F}{\partial \xi} \\ \dfrac{\partial F}{\partial \eta} \end{Bmatrix} = \begin{bmatrix} \dfrac{\partial \xi}{\partial \xi^*} & \dfrac{\partial \eta}{\partial \xi^*} \\ 0 & \dfrac{\partial \eta}{\partial \eta^*} \end{bmatrix} \begin{Bmatrix} \dfrac{\partial F}{\partial \xi} \\ 0 \end{Bmatrix} = \begin{Bmatrix} \dfrac{\partial \xi}{\partial \xi^*} \dfrac{\partial F}{\partial \xi} \\ 0 \end{Bmatrix} \tag{B.4}$$

In this special case $\partial\xi/\partial\xi^*$ is a constant, and $\partial F/\partial\xi$ is independent of η, so

$$\frac{\partial F(\varphi_{00})}{\partial \xi^*} = \frac{\partial F(\varphi_{01})}{\partial \xi^*}, \quad \frac{\partial F(\varphi_{10})}{\partial \xi^*} = \frac{\partial F(\varphi_{11})}{\partial \xi^*} \tag{B.5}$$

The second derivative of F is expressed as:

$$\frac{\partial^2 F}{\partial \xi^* \partial \eta^*} = \partial\left(\frac{\partial \xi}{\partial \xi^*}\frac{\partial F}{\partial \xi}\right) / \partial \eta^* = \frac{\partial \xi}{\partial \xi^*}\frac{\partial \eta}{\partial \eta^*}\frac{\partial^2 F}{\partial \xi \partial \eta} = 0 \tag{B.6}$$

It should be noted that in the above derivation, the relation $\partial^2\xi/\partial\xi^*\partial\eta^* = \xi_{00} - \xi_{10} - \xi_{10} + \xi_{11} = 0$ is used.

$$\frac{\partial^2 F}{\partial \xi \partial \eta} = \sum_{k=1}^{6} \frac{\partial^2 N_k}{\partial \xi \partial \eta} |\varphi_k| = 0 \tag{B.7}$$

In the above derivation, the following relations are used:

$$|\varphi_1| = |\varphi_3| = |\varphi_6| = c, \quad |\varphi_4| = |\varphi_5| = |0.5 - c|, \quad |\varphi_2| = 1 - c \tag{B.8}$$

Set $F(\varphi_{00}) = F(\varphi_{01}) = a$, $F(\varphi_{10}) = F(\varphi_{11}) = b$, $\partial F(\varphi_{00})/\partial\xi^* = \partial F(\varphi_{01})/\partial\xi^* = e$, $\partial F(\varphi_{01})/\partial\xi^* = \partial F(\varphi_{11})/\partial\xi^* = f$. Hence, $\mathbf{G}_\mathrm{t}$ is of the form:

$$\mathbf{G}_\mathrm{t} = \begin{bmatrix} a & a & e & e \\ b & b & f & f \\ 0 & 0 & 0 & 0 \\ 0 & 0 & 0 & 0 \end{bmatrix} \tag{B.9}$$

and $\mathbf{M}^\mathrm{T}\mathbf{G}_\mathrm{t}\mathbf{M}$ is of the form:

$$\mathbf{M}^{\mathrm{T}}\cdot\mathbf{G}_{\mathrm{t}}\cdot\mathbf{M}=\begin{bmatrix} a & 0 & 0 & 0 \\ 0 & 0 & 0 & 0 \\ -3a+3b-2e-f & 0 & 0 & 0 \\ 2a-2b+e+f & 0 & 0 & 0 \end{bmatrix} \tag{B.10}$$

The terms appear in $\mathbf{H}_{\mathrm{t}}$ are shown in Table A1 with underlines. It can be seen that the degree of the complete polynomial is 0, and in this case, the degree of the complete polynomial of the interpolation function for additional translational DOF is 2.

Case 2: the yield line is parallel to the hypotenuse of the triangle element in the natural coordinate (Figure B1)

In this case, the center line of the yield line is parallel to the hypotenuse, as shown in Figure B1. The location of the yield line can be expressed as

$$\varphi=\xi+\eta-c=0 \tag{B.11}$$

Therefore, the enrichment for the non-Hermitian area is written as

$$F=\sum_{k=1}^{6}N_k\left|\varphi_k\right|-\left|\sum_{k=1}^{6}\varphi_k N_k\right|$$

$$=c\left(1-2\xi-2\eta\right)+\left(\xi+\eta\right)\left(2\xi+2\eta-1\right)+4\left|0.5-c\right|\left(\xi+\eta\right)\left(1-\xi-\eta\right)-\left|\xi+\eta-c\right| \tag{B.12}$$

Set $\xi+\eta=\rho$, the enrichment function F can be rewritten as:

$$F=c\left(1-2\rho\right)+\rho\left(2\rho-1\right)+4\left|0.5-c\right|\rho\left(1-\rho\right)-\left|\rho-c\right| \tag{B.13}$$

Since $\rho_{00}=\rho_{10}$, $\rho_{01}=\rho_{11}$, set

$$F\left(\varphi_{00}\right)=F\left(\varphi_{10}\right)=a\,,\; F\left(\varphi_{01}\right)=F\left(\varphi_{11}\right)=b \tag{B.14}$$

$$\begin{pmatrix} \dfrac{\partial F}{\partial \xi^*} \\ \dfrac{\partial F}{\partial \eta^*} \end{pmatrix}=\begin{bmatrix} \dfrac{\partial \xi}{\partial \xi^*} & \dfrac{\partial \eta}{\partial \xi^*} \\ \dfrac{\partial \xi}{\partial \eta^*} & \dfrac{\partial \eta}{\partial \eta^*} \end{bmatrix}\begin{pmatrix} \dfrac{\partial F}{\partial \xi} \\ \dfrac{\partial F}{\partial \eta} \end{pmatrix}=\begin{bmatrix} \xi_{10}+\sqrt{2}\omega_e\eta^* & -\eta_{00}-\sqrt{2}\omega_e\eta^* \\ \sqrt{2}\omega_e\xi^* & \sqrt{2}\left(1-\xi^*\right)\omega_e \end{bmatrix}\begin{pmatrix} \dfrac{\partial F}{\partial \xi} \\ \dfrac{\partial F}{\partial \eta} \end{pmatrix} \tag{B.15}$$

Because of the symmetry of variables ξ and η in the expression of F, $\partial F/\partial\xi = \partial F/\partial\eta$. On the other hand, $\xi_{10} = \eta_{00}$. Therefore, $\partial F/\partial\xi^{*} = 0$. Furthermore, $\partial^{2}F/\partial\xi^{*}\partial\eta^{*} = 0$.

Set

$$\left.\frac{\partial F}{\partial \xi}\right|_{\substack{\rho=\rho_{10}\\ \rho=\rho_{00}}} = \left.\frac{\partial F}{\partial \eta}\right|_{\substack{\rho=\rho_{10}\\ \rho=\rho_{00}}} = -2c + 4\rho - 1 + 4\left|0.5 - c\right|\left(1-2\rho\right) - 1 = e \tag{B.16}$$

$$\left.\frac{\partial F}{\partial \xi}\right|_{\substack{\rho=\rho_{11}\\ \rho=\rho_{01}}} = \left.\frac{\partial F}{\partial \eta}\right|_{\substack{\rho=\rho_{11}\\ \rho=\rho_{01}}} = -2c + 4\rho - 1 + 4\left|0.5 - c\right|\left(1-2\rho\right) + 1 = f \tag{B.17}$$

and

$$\sqrt{2}\omega_{e} = l \tag{B.18}$$

Substitute Equation (B.16), Equation (B.17) and Equation (B.18) into Equation (B.15):

$$\begin{pmatrix} \dfrac{\partial F}{\partial \xi^{*}} \\ \dfrac{\partial F}{\partial \eta^{*}} \end{pmatrix}_{00} = \begin{pmatrix} 0 \\ 2le \end{pmatrix}, \begin{pmatrix} \dfrac{\partial F}{\partial \xi^{*}} \\ \dfrac{\partial F}{\partial \eta^{*}} \end{pmatrix}_{01} = \begin{pmatrix} 0 \\ 2lf \end{pmatrix}, \begin{pmatrix} \dfrac{\partial F}{\partial \xi^{*}} \\ \dfrac{\partial F}{\partial \eta^{*}} \end{pmatrix}_{10} = \begin{pmatrix} 0 \\ le \end{pmatrix}, \begin{pmatrix} \dfrac{\partial F}{\partial \xi^{*}} \\ \dfrac{\partial F}{\partial \eta^{*}} \end{pmatrix}_{11} = \begin{pmatrix} 0 \\ 2lf \end{pmatrix} \tag{B.19}$$

Hence, $\mathbf{G}_{\mathrm{t}}$ is of the form:

$$\mathbf{G}_{\mathrm{t}} = \begin{bmatrix} a & b & 2le & 2lf \\ a & b & le & 2lf \\ 0 & 0 & 0 & 0 \\ 0 & 0 & 0 & 0 \end{bmatrix} \tag{B.20}$$

and $\mathbf{M}^{\mathrm{T}}\mathbf{G}_{\mathrm{t}}\mathbf{M}$ is of the form:

$$\mathbf{M}^{\mathrm{T}}\mathbf{G}_{\mathrm{t}}\mathbf{M} = \begin{bmatrix} a & 2le & 3\left(b-a\right)-2l\left(2e+f\right) & 2\left(a-b\right)+2l\left(e+f\right) \\ 0 & 0 & 0 & 0 \\ 0 & -3le & 6le & -3le \\ 0 & 2le & -4le & 2le \end{bmatrix} \tag{B. 21}$$

The terms appear in $\mathbf{H}_t$ are shown in Table B2 with underlines. It can be seen that the degree of the complete polynomial is 0, and in this case, the degree of the complete polynomial of the interpolation function for additional translational DOF is 2.

Case 3: the yield line is perpendicular to the hypotenuse (Figure B2)

It is shown in Figure B2 that the yield line is perpendicular to the hypotenuse and passes through one of the corner point. The location of the yield line is expressed as

$$\varphi = \xi - \eta - 1 = 0 \tag{B.22}$$

The enrichment for the non-Hermitian area is written as

$$F = \sum_{k=1}^{6} N_k \left|\varphi_k\right| - \left|\sum_{k=1}^{6} \varphi_k N_k\right| = 1 - \xi - \eta - \left|1 - \xi - \eta\right| \tag{B.23}$$

Therefore, $F(\varphi_{00}) = F(\varphi_{01}) = 0$, $\partial F(\varphi_{00}) / \partial\xi^* = \partial F(\varphi_{01}) / \partial\xi^* = 0$, $\partial F(\varphi_{00}) / \partial\eta^* = \partial F(\varphi_{01}) / \partial\eta^* = 0$ and $\partial^2 F(\varphi_{00}) / \partial\xi^*\partial\eta^* = \partial^2 F(\varphi_{01}) / \partial\xi^*\partial\eta^* = 0$.

Hence, the terms in the Hermite function are shown in Table B3 with underlines. It can be seen that there is no complete polynomial in the Hermite function in this case.

Case 4: the yield line is perpendicular to the hypotenuse (Figure B3)

As shown in Figure B3, the yield line is perpendicular to the hypotenuse and the center of the HGZ passes through the right angle ($\angle 312$).

The location of the yield line is expressed as:

$$\varphi = \xi - \eta = 0 \tag{B.24}$$

The enrichment for the non-Hermitian area is written as

$$F = \sum_{k=1}^{6} N_k \left|\varphi_k\right| - \left|\sum_{k=1}^{6} \varphi_k N_k\right| = \xi - 4\xi\eta + \eta - \left|\xi - \eta\right| \tag{B.25}$$

Therefore, $F(\varphi_{00}) = F(\varphi_{10}) = 0$ and the constant term does not appear in the Hermite function in this case and there is no complete polynomial in the Hermite function in this case.

Finally, it can be concluded that in all the above cases, the 3 × 3 Gaussian integration scheme is sufficient for the convergence condition [33].

Reference

[1] Fries, T.-P. and T. Belytschko. The extended/generalized finite element method: An overview of the method and its applications. *International Journal for Numerical Methods in Engineering* 2010; **84(3)**: 253-304.

[2] Belytschko, T. and T. Black. Elastic crack growth in finite elements with minimal remeshing. *International Journal for Numerical Methods in Engineering* 1999; **45(5)**: 601-620.

[3] Moës, N., J. Dolbow and T. Belytschko. A finite element method for crack growth without remeshing. *International Journal for Numerical Methods in Engineering* 1999; **46(1)**: 131-150.

[4] Sukumar, N., D.L. Chopp, N. Moës and T. Belytschko. Modeling holes and inclusions by level sets in the extended finite-element method. *Computer Methods in Applied Mechanics and Engineering* 2001; **190(46-47)**: 6183-6200.

[5] Zi, G. and T. Belytschko. New crack-tip elements for XFEM and applications to cohesive cracks. *International Journal for Numerical Methods in Engineering* 2003; **57(15)**: 2221-2240.

[6] Moës, N., M. Cloirec, P. Cartraud and J.F. Remacle. A computational approach to handle complex microstructure geometries. *Computer Methods in Applied Mechanics and Engineering* 2003; **192(28-30)**: 3163-3177.

[7] Areias, P.M.A. and T. Belytschko. Two-scale shear band evolution by local partition of unity. *International Journal for Numerical Methods in Engineering* 2006; **66(5)**: 878-910.

[8] Rabczuk, T., P.M.A. Areias and T. Belytschko. A simplified mesh-free method for shear bands with cohesive surfaces. *International Journal for Numerical Methods in Engineering* 2007; **69(5)**: 993-1021.

[9] Rabczuk, T. and E. Samaniego. Discontinuous modelling of shear bands using adaptive meshfree methods. *Computer Methods in Applied Mechanics and Engineering* 2008; **197(6–8)**: 641-658.

[10] Benvenuti, E., A. Tralli and G. Ventura. A regularized XFEM model for the transition from continuous to discontinuous displacements. *International Journal for Numerical Methods in Engineering* 2008; **74(6)**: 911-944.

[11] Areias, P.M.A. and T. Belytschko. Non-linear analysis of shells with arbitrary evolving cracks using XFEM. *International Journal for Numerical Methods in Engineering* 2005; **62(3)**: 384-415.

[12] Areias, P.M.A. and T. Belytschko. Analysis of three-dimensional crack initiation and propagation using the extended finite element method. *International Journal for Numerical Methods in Engineering* 2005; **63(5)**: 760-788.

[13] Stazi, F.L., E. Budyn, J. Chessa and T. Belytschko. An extended finite element method with higher-order elements for curved cracks. *Computational Mechanics* 2003; **31(1)**: 38-48.

[14] Belytschko, T. and R. Gracie. On XFEM applications to dislocations and interfaces. *International Journal of Plasticity*; **23(10-11)**: 1721-1738.

[15] Natarajan, S., P.M. Baiz, S. Bordas, T. Rabczuk and P. Kerfriden. Natural frequencies of cracked functionally graded material plates by the extended finite element method. *Composite Structures* 2011; **93(11)**: 3082-3092.

[16] P.M., B., N. S., B. S., K. P. and R. T. Linear buckling analysis of cracked plates by SFEM and XFEM (SmXFEM). *Journal of Mechanics of Materials and Structures* 2012; **6(9-10)**: 1213-1238.

[17] Xu, J., C.K. Lee and K.H. Tan. A two-dimensional co-rotational Timoshenko beam element with XFEM formulation. *Computational Mechanics* 2012; **49(5)**: 667-683.

[18] Rabczuk, T., P.M.A. Areias and T. Belytschko. A meshfree thin shell method for non-linear dynamic fracture. *International Journal for Numerical Methods in Engineering* 2007; **72(5)**: 524-548.

[19] T., R. and A. P.M.A. A Meshfree Thin Shell for Arbitrary Evolving Cracks Based on An Extrinsic Basis. *CMES: Computer Modeling in Engineering and Sciences* 2006; **16(2)**: 115-130.

[20] Rabczuk, T., R. Gracie, J.-H. Song and T. Belytschko. Immersed particle method for fluid–structure interaction. *International Journal for Numerical Methods in Engineering* 2010; **81(1)**: 48-71.

[21] Chau-Dinh, T., G. Zi, P.-S. Lee, T. Rabczuk and J.-H. Song. Phantom-node method for shell models with arbitrary cracks. *Computers & Structures* 2012; **92–93(0)**: 242-256.

[22] Fries, T.-P. A corrected XFEM approximation without problems in blending elements. *International Journal for Numerical Methods in Engineering* 2008; **75(5)**: 503-532.

[23] Zienkiewicz, O.C. and R.L. Taylor. *Finite Element Method (6th Edition) Volume 2 - Solid Mechanics*, 2005, Elsevier.

[24] Bletzinger, K.-U., M. Bischoff and E. Ramm. A unified approach for shear-locking-free triangular and rectangular shell finite elements. *Computers & Structures* 2000; **75(3)**: 321-334.

[25] Lee, P.-S. and K.-J. Bathe. Development of MITC isotropic triangular shell finite elements. *Computers & Structures* 2004; **82(11-12)**: 945-962.

[26] Beirão da Veiga, L., D. Chapelle and I. Paris Suarez. Towards improving the MITC6 triangular shell element. *Computers & Structures* 2007; **85(21-22)**: 1589-1610.

[27] Nguyen-Xuan, H., T. Rabczuk, N. Nguyen-Thanh, T. Nguyen-Thoi and S. Bordas. A node-based smoothed finite element method with stabilized discrete shear gap technique for analysis of Reissner–Mindlin plates. *Computational Mechanics* 2010; **46(5)**: 679-701.

[28] Owen DRJ, H.E. *Finite element in plasticity, theory and practice*. 1 ed Pineridge Press, Swansea, 1980.

[29] Crisfield, M.A. *Non-Linear Finite Element Analysis of Solids and Structures, Volume 1, Essentials*. 1 ed John Wiley & Sons: Chichester, 1991.

[30] Simo, J.C. and T.J.R. Hughes. *Computational Inelasticity* Springer: New York, 1998.

[31] Crisfield, M.A. *Non-Linear Finite Element Analysis of Solids and Structures, Volume 2, Advanced topics*. 1 ed John Wiley & Sons: Chichester, 1991.

[32] Budkowska, B.B. and Q. Fu. Analytical determination of the optimal strain and stress points for the displacement model of the finite element method. *Computers & Structures* 1991; **41(5)**: 937-946.
[33] Zienkiewicz, O.C. and R.L. Taylor. *Finite Element Method (5th Edition) Volume 1 - The Basis*, 2000, Elsevier.
[34] *ANSYS 11.0 Manual*.
[35] Johansen, K.W. *Yield-line formulae for slabs* Taylor & Francis, 1972.

Table 1 The three cases of example 1

	thickness t	yield strength σ_y	reference loading q_0	thickness/length ratio t / L
Case 1	0.5	0.4	6.4×10^{-2}	1 / 10
Case 2	0.25	0.2	8×10^{-3}	1 / 20
Case 3	0.125	0.1	1×10^{-3}	1 / 40
Case 4	0.05	0.04	6.4×10^{-5}	1 / 100
Case 5	0.01	0.008	5.12×10^{-7}	1 / 500

Table A1 The polynomials in the enrichment F in non HGZ and the integration scheme required

Case	terms appear in F						degree of complete polynomial in interpolation function	minimal order of integration scheme
	1	ξ	η	ξ^2	$\xi\eta$	η^2		
s1s3	√	√	√	√	√		3	3 × 3
s1s4	√	√	√	√	√		3	3 × 3
s1s5	√	√	√	√	√	√	4	4 × 4
s1s6	√	√	√	√	√	√	4	4 × 4
s2s3	√	√	√	√			3	3 × 3
s2s4	√	√	√	√	√		3	3 × 3
s2s5	√	√	√	√	√	√	4	4 × 4
s2s6	√	√	√	√	√	√	4	4 × 4
s3s6	√	√	√		√	√	3	3 × 3
s4s6	√	√	√		√	√	3	3 × 3
s3s5	√	√	√			√	3	3 × 3
s4s5	√	√	√		√	√	3	3 × 3

Table B1 The polynomial terms in $\mathbf{H}_t$ when the yield line is parallel to one of the catheti

			$\underline{1}$				--- 0
		ξ^*		η^*			--- 1
	$\underline{\xi^{*2}}$		$\xi^*\eta^*$		η^{*2}		--- 2
$\underline{\xi^{*3}}$		$\xi^{*2}\eta^*$		$\xi^*\eta^{*2}$		η^{*3}	--- 3
	$\xi^{*3}\eta^*$		$\xi^{*2}\eta^{*2}$		$\xi^*\eta^{*3}$		--- 4
		$\xi^{*3}\eta^{*2}$		$\xi^{*2}\eta^{*3}$			--- 5
			$\xi^{*3}\eta^{*3}$				--- 6

Table B2 The polynomial terms in $\mathbf{H}_t$ when the yield line is parallel to the hypotenuse

			$\underline{1}$				--- 0
		ξ^*		$\underline{\eta^*}$			--- 1
	ξ^{*2}		$\xi^*\eta^*$		$\underline{\eta^{*2}}$		--- 2
ξ^{*3}		$\underline{\xi^{*2}\eta^*}$		$\xi^*\eta^{*2}$		$\underline{\eta^{*3}}$	--- 3
	$\underline{\xi^{*3}\eta^*}$		$\underline{\xi^{*2}\eta^{*2}}$		$\xi^*\eta^{*3}$		--- 4
		$\underline{\xi^{*3}\eta^{*2}}$		$\underline{\xi^{*2}\eta^{*3}}$			--- 5
			$\underline{\xi^{*3}\eta^{*3}}$				--- 6

Table B3 The polynomial terms in $\mathbf{H}_t$ when the yield line is perpendicular to the hypotenuse and passes through one of the corner point

			1				--- 0
		ξ^*		η^*			--- 1
	$\underline{\xi^{*2}}$		$\xi^*\eta^*$		η^{*2}		--- 2
$\underline{\xi^{*3}}$		$\xi^{*2}\eta^*$		$\xi^*\eta^{*2}$		η^{*3}	--- 3
	$\xi^{*3}\eta^*$		$\underline{\xi^{*2}\eta^{*2}}$		$\xi^*\eta^{*3}$		--- 4
		$\underline{\xi^{*3}\eta^{*2}}$		$\underline{\xi^{*2}\eta^{*3}}$			--- 5
			$\underline{\xi^{*3}\eta^{*3}}$				--- 6

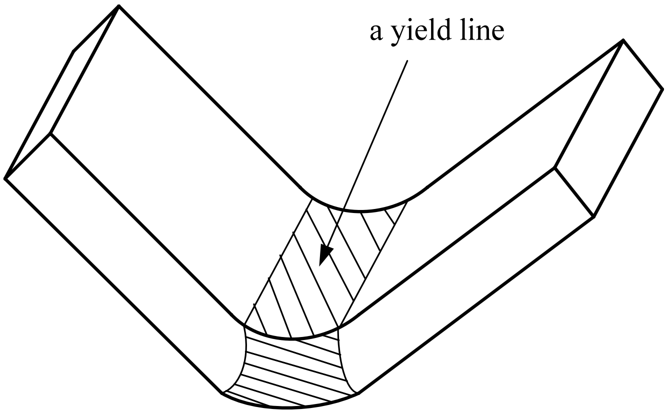

Figure 1 Non-smoothness near a yield line in a plate

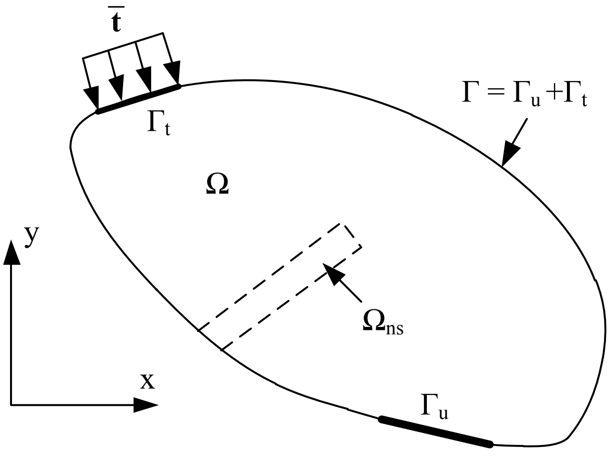

Figure 2 Domain definition

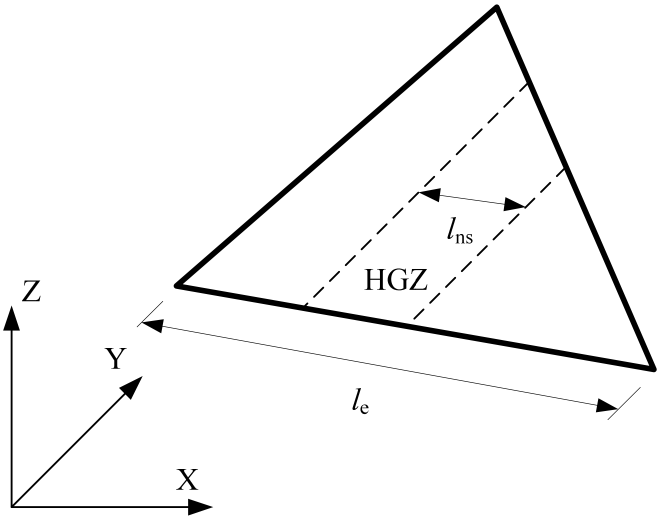

a) The physical width of a HGZ (l_{ns}) and the physical length of an enriched element (l_e)

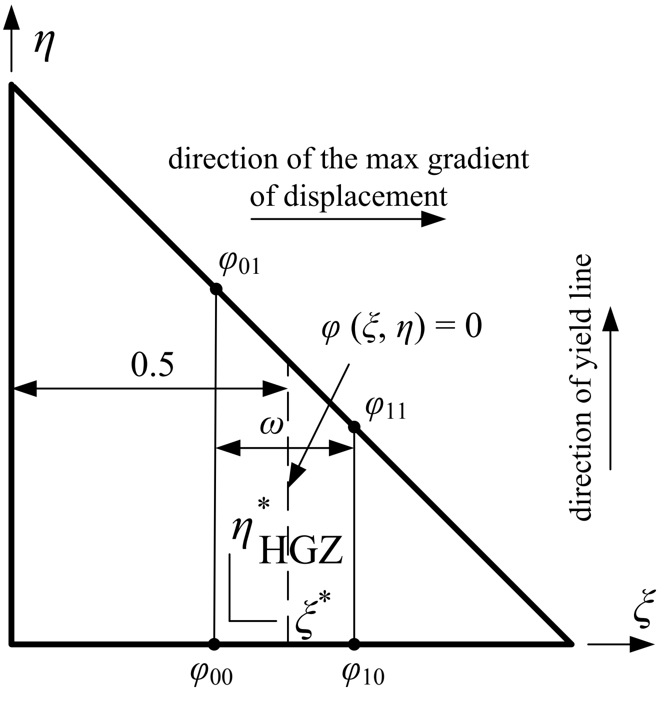

b) A triangular element with a HGZ and the parametric width of a HGZ (ω)

Figure 3 The definition of HGZ and the width of a HGZ

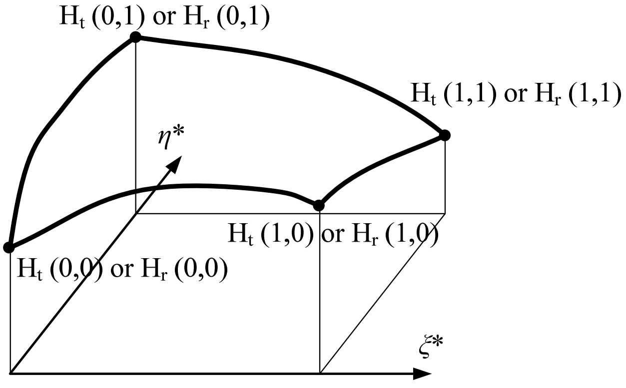

Figure 4 The parent coordinate system for HGZ

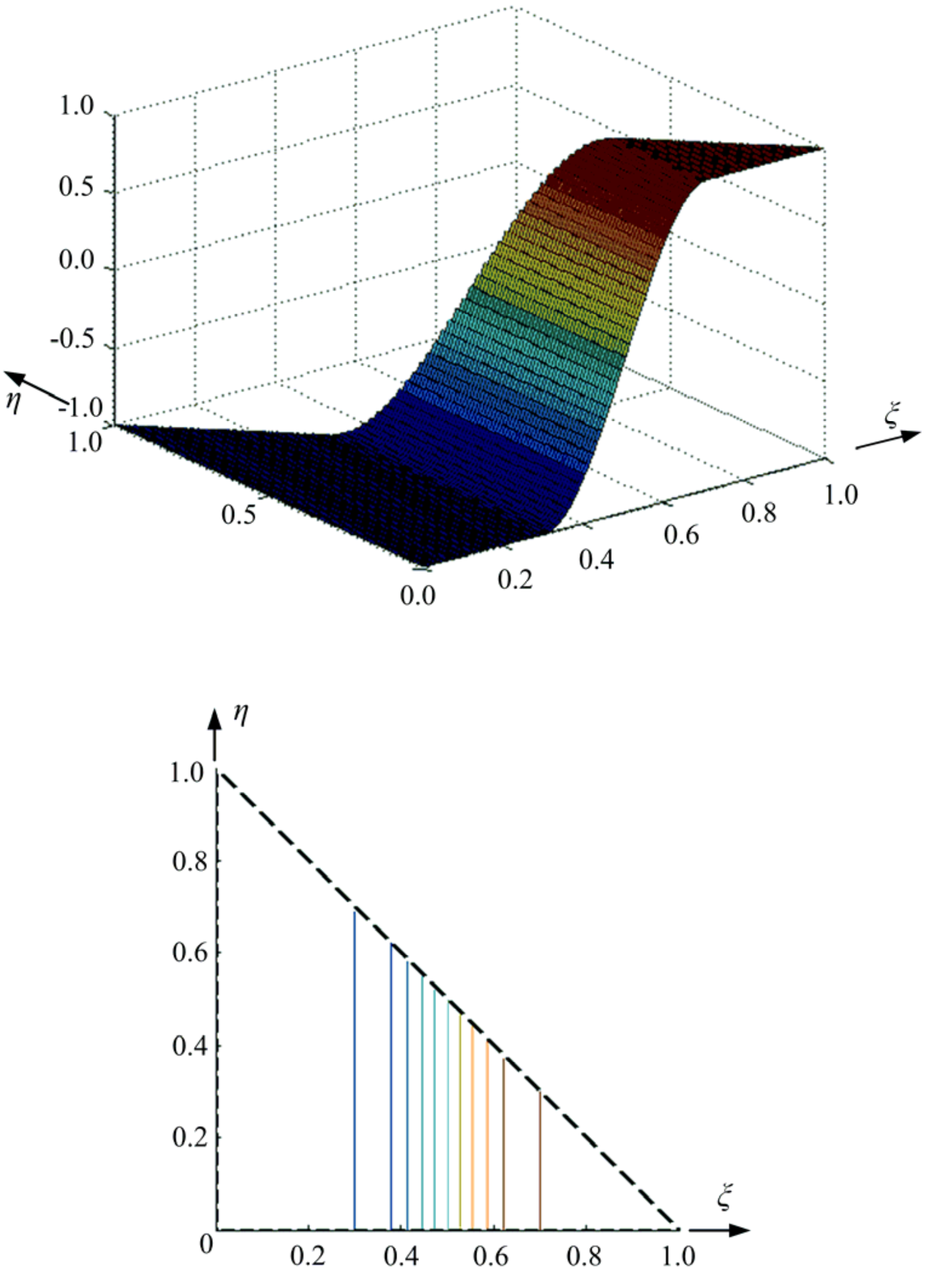

(a) The 3D plot of R

(b) The contour of R

Figure 5 The plot of R

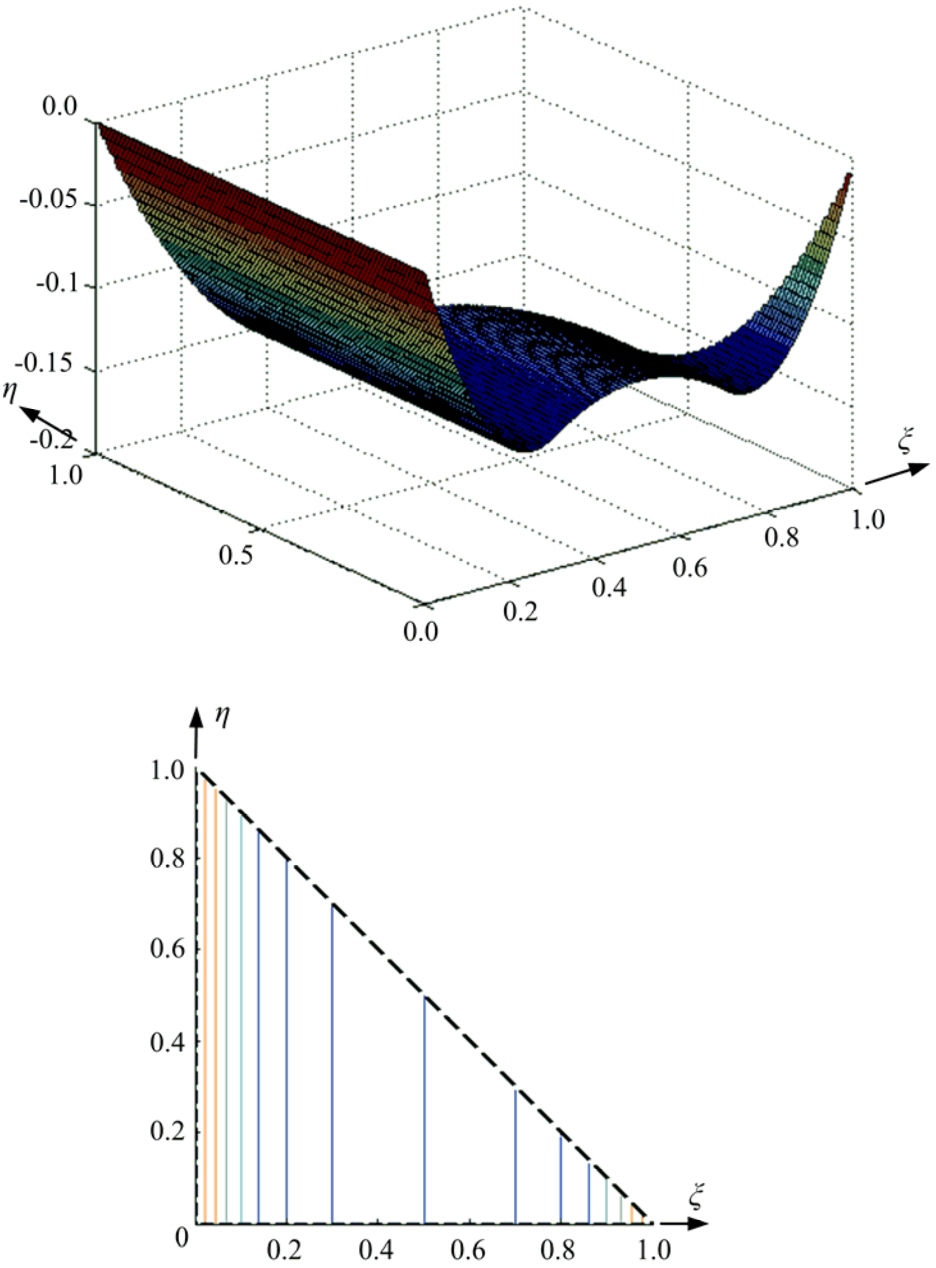

(a) The 3D plot of *F*

(b) The contour of *F*

Figure 6 The plot of *F*

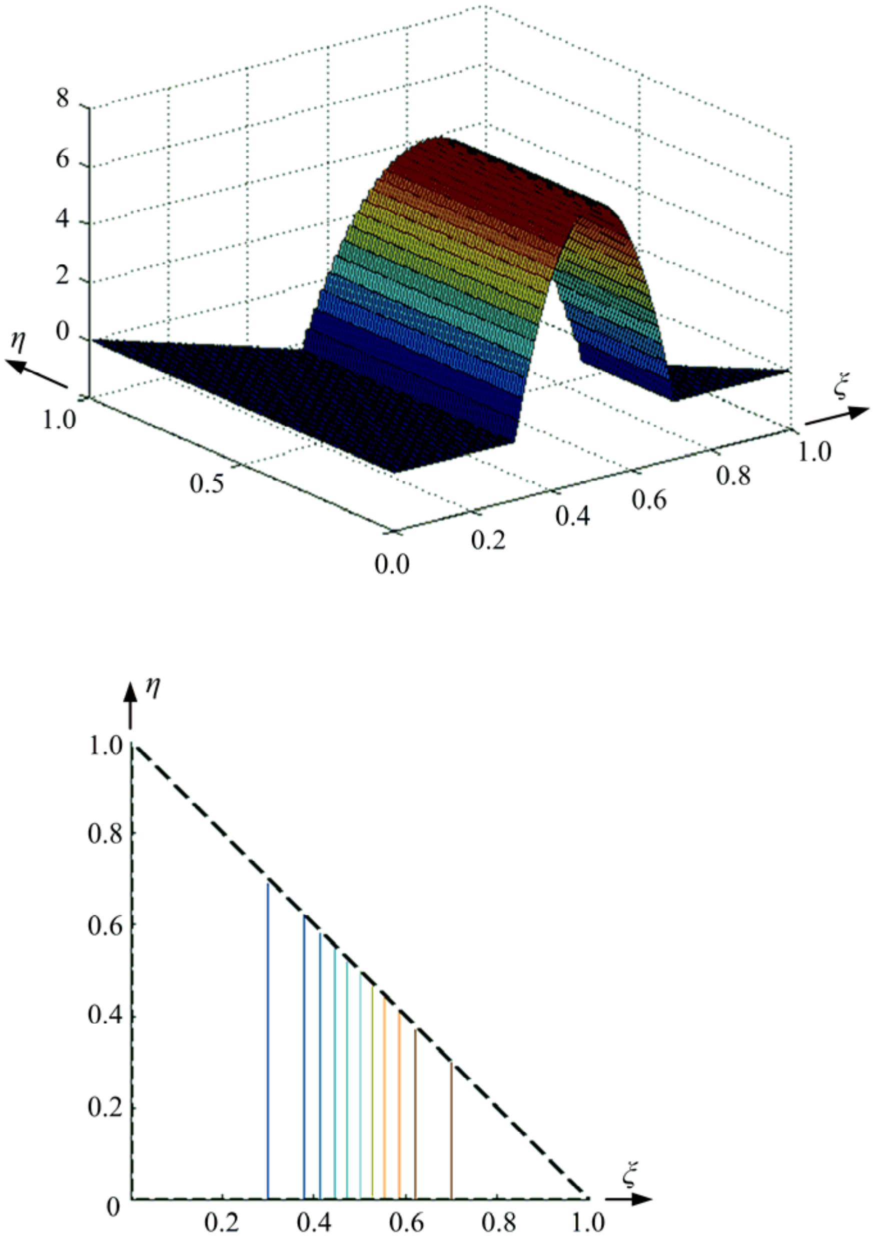

(a) The 3D plot of $S_{i,\xi}$

(b) The contour of $S_{i,\xi}$

Figure 7 The plot of $S_{i,\xi}$

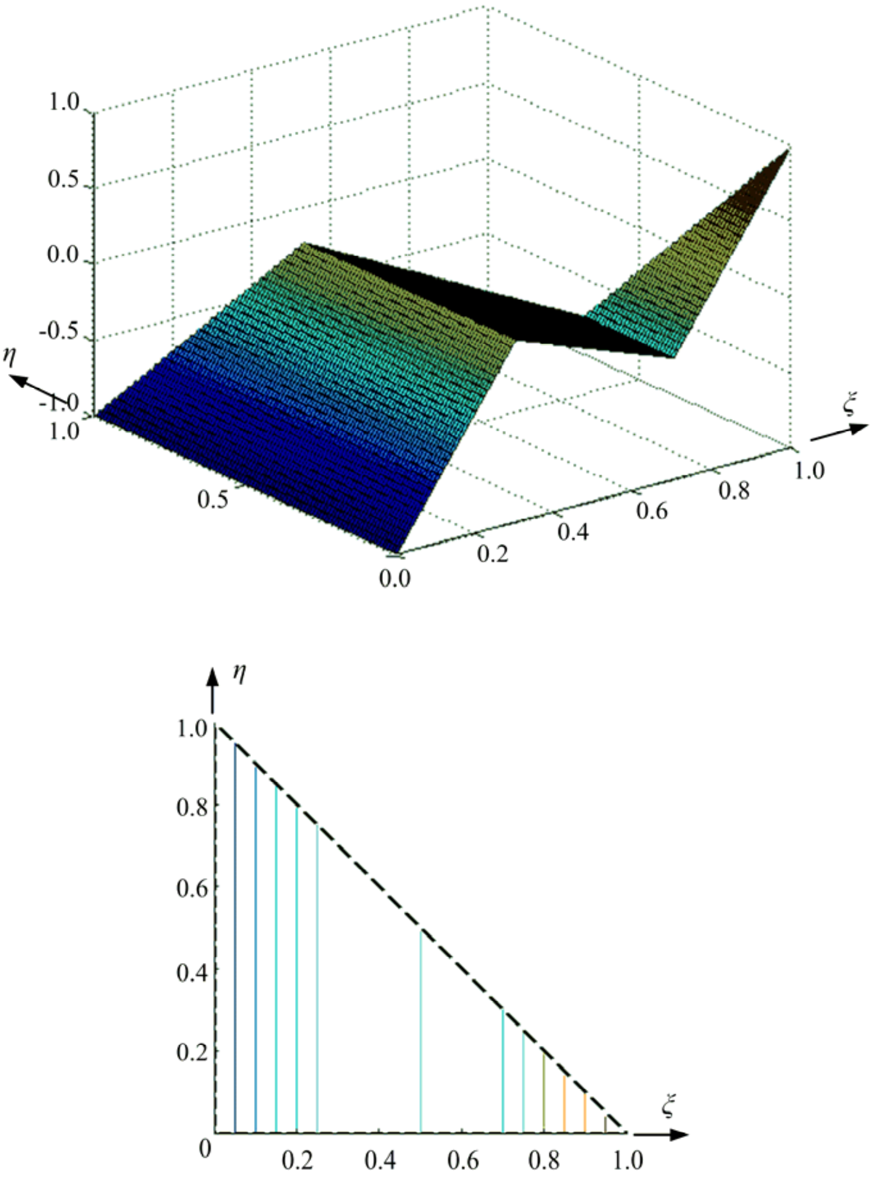

(a) The 3D plot of $F_{,\xi}$

(b) The contour of $F_{,\xi}$

Figure 8 The plot of $F_{,\xi}$

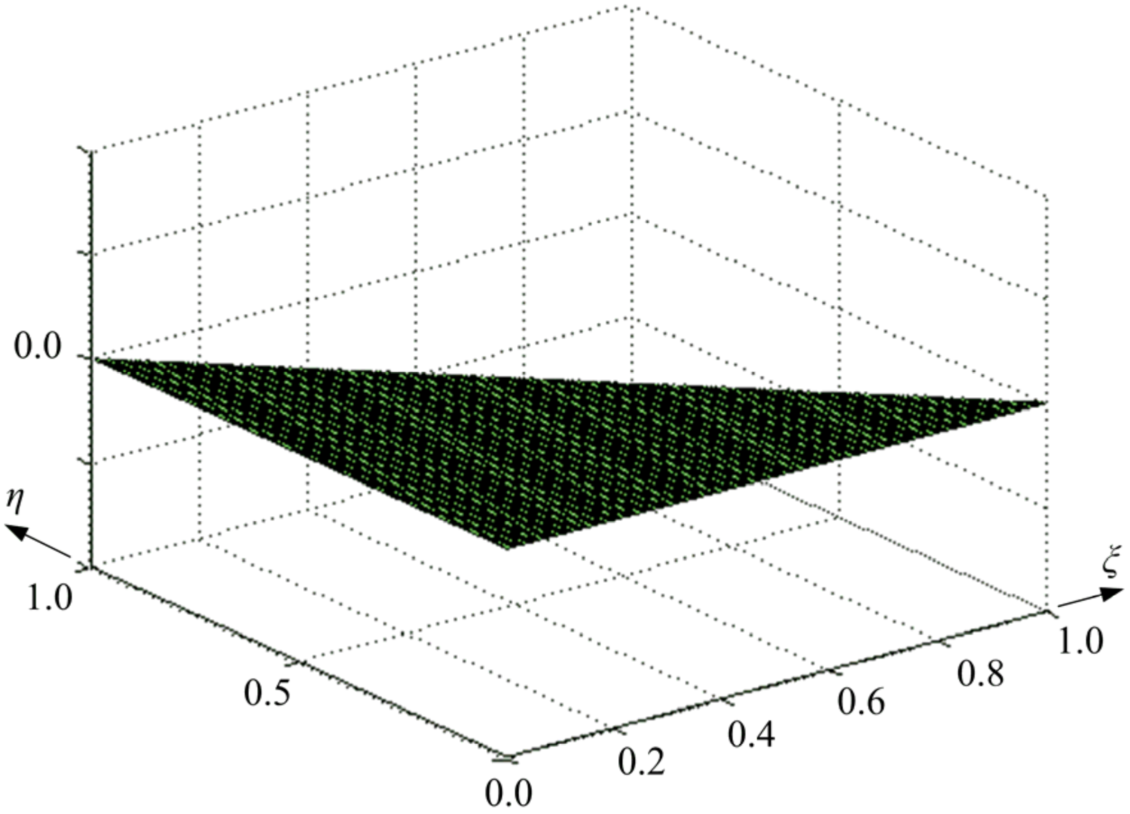

Figure 9 The plot of $S_{i,\eta}$, $F_{,\eta}$

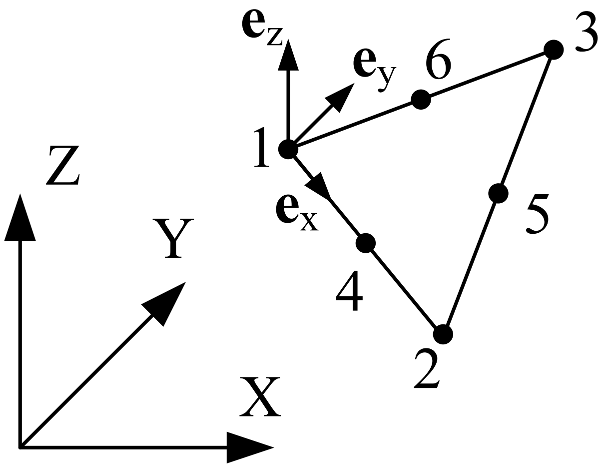

Figure 10 The local and global coordinate system of the plate element

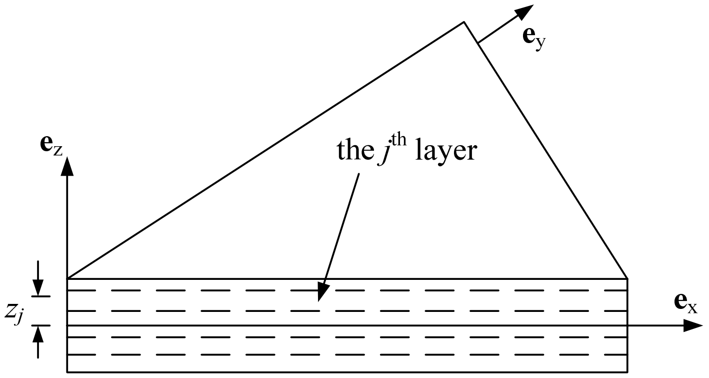

Figure 11 The layered model for the plate element

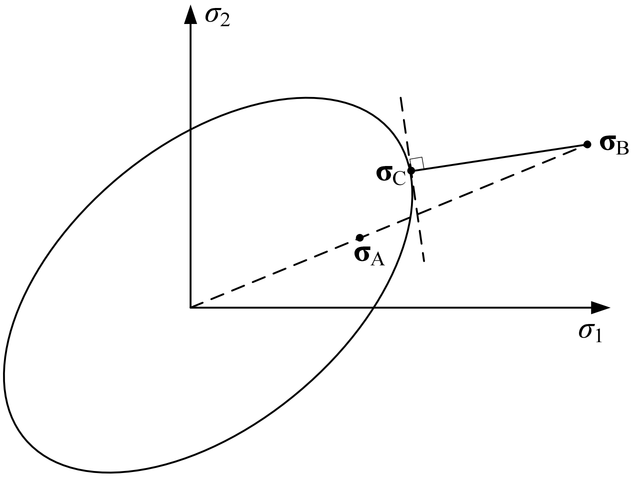

Figure 12 The Backward Euler algorithm

(a) 1 QUnH + 1TRnH+ 1 TRH

(b) 1 QUnH + 1 TRH

(c) 1 TRnH + 1 QUH

(d) 2 TRnH + 2 QUH

Figure 13 Partition of an enriched element

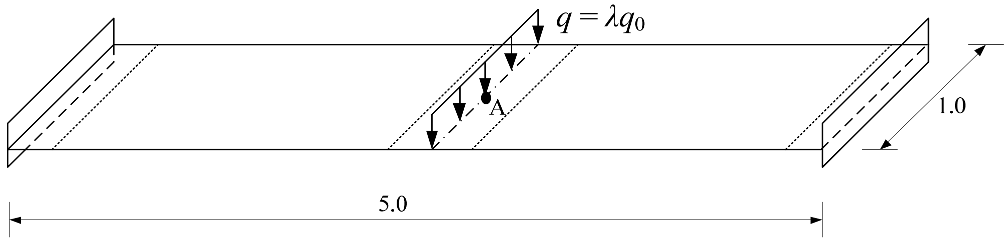

Figure 14 Example 1: A flat strip with two fully fixed ends

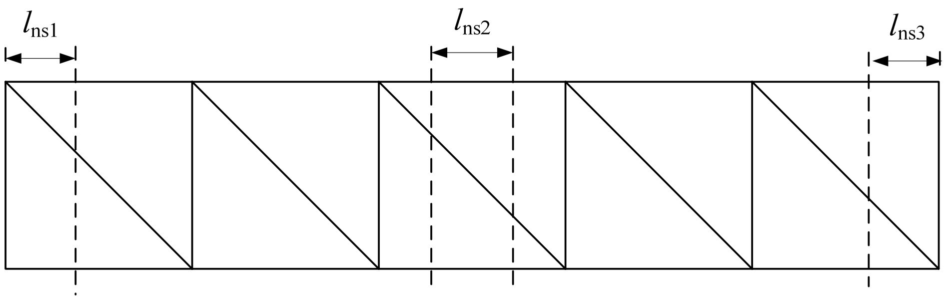

Figure 15 The mesh scheme and the locations of the three possible yield lines

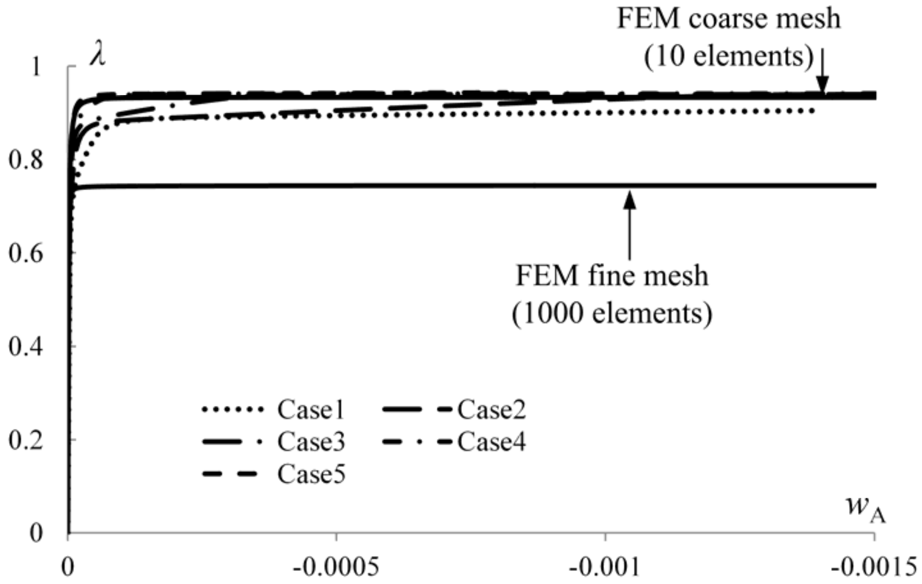

Figure 16 The equilibrium path obtained for Example 1 by full integration

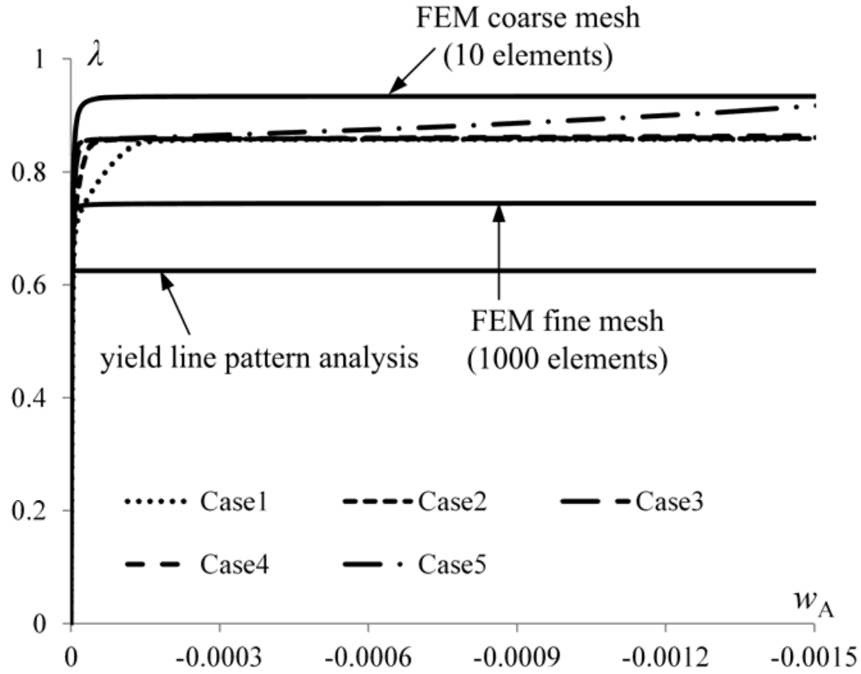

Figure 17 The equilibrium path obtained for Example 1 by reduced integration

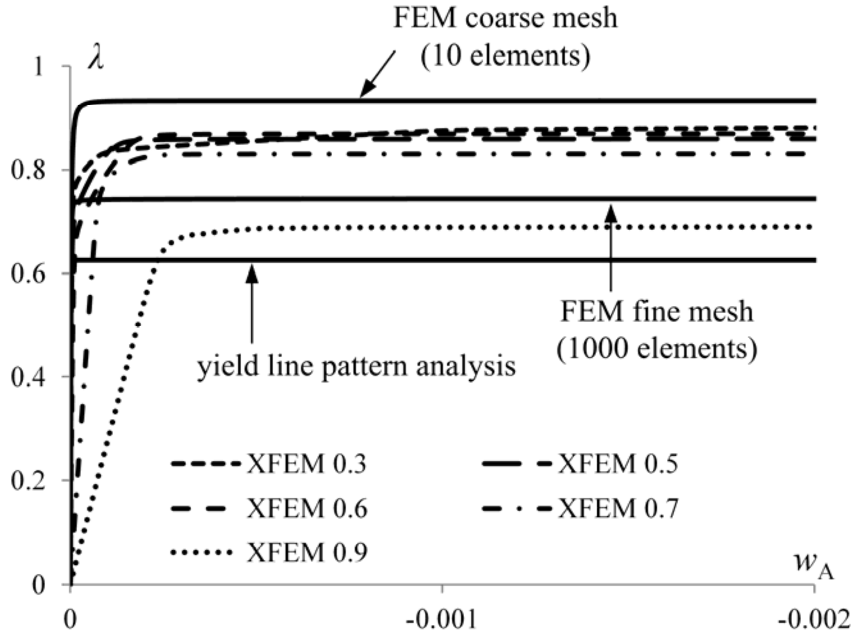

Figure 18 The equilibrium path obtained for Example 1 with variation of ω_2

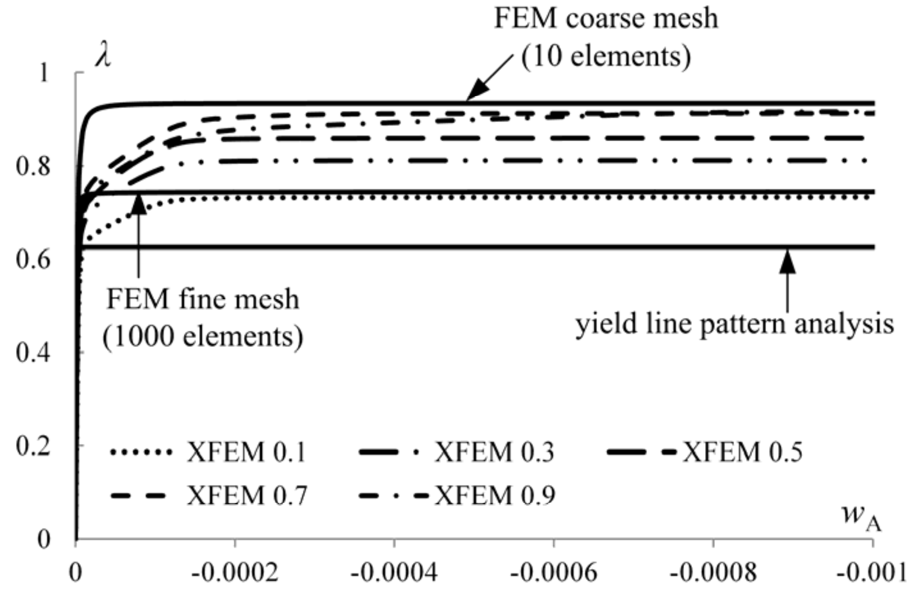

Figure 19 The equilibrium paths obtained for Example 1 with variation of ω_1 and ω_3

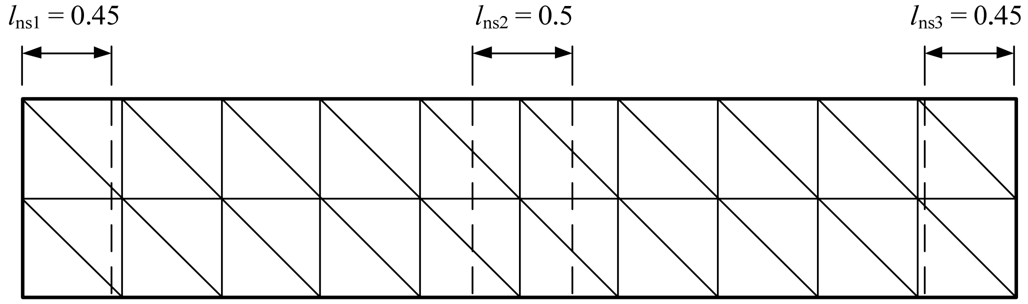

Figure 20 A refined mesh (mesh 2) for Example 1

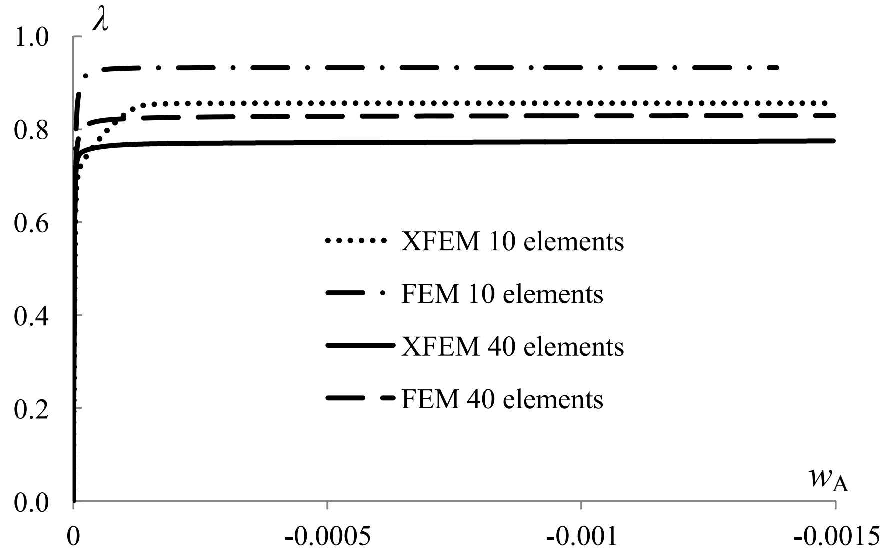

Figure 21 The equilibrium paths obtained for Example 1 with a refined mesh

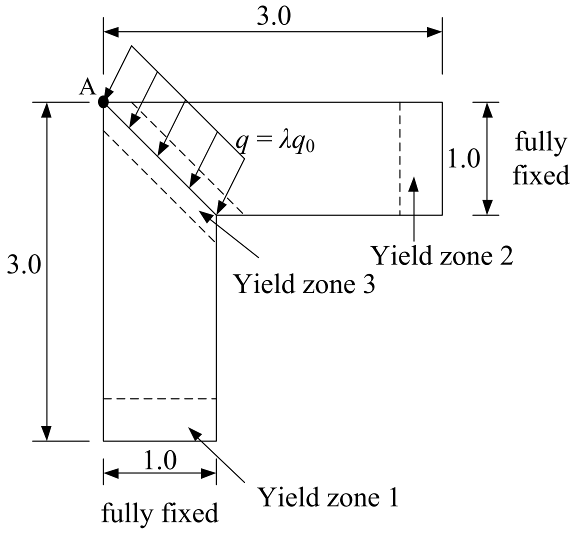

Figure 22 Example 2: An L-shaped plate with two fully fixed ends

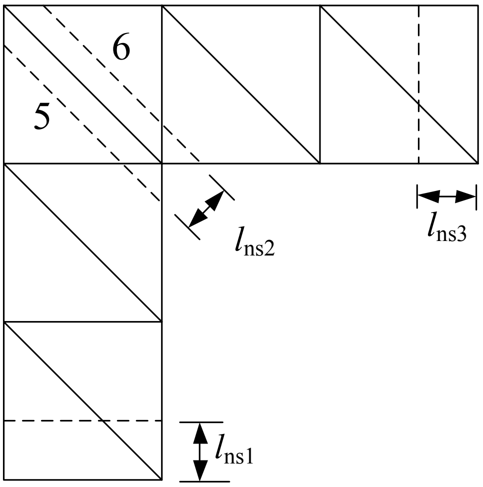

Figure 23 The mesh scheme of Example 2

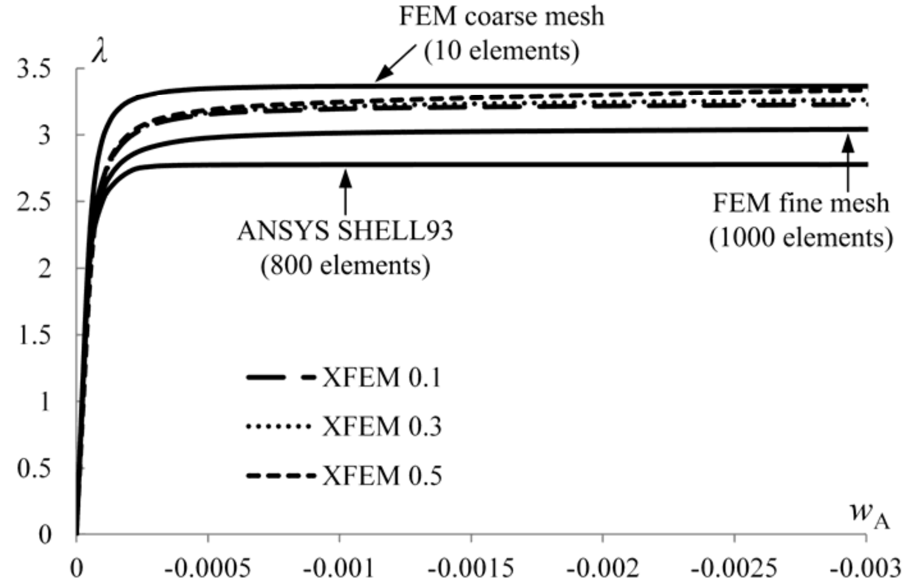

Figure 24 The equilibrium paths obtained for Example 2 with variation of l_{ns1} and l_{ns3}

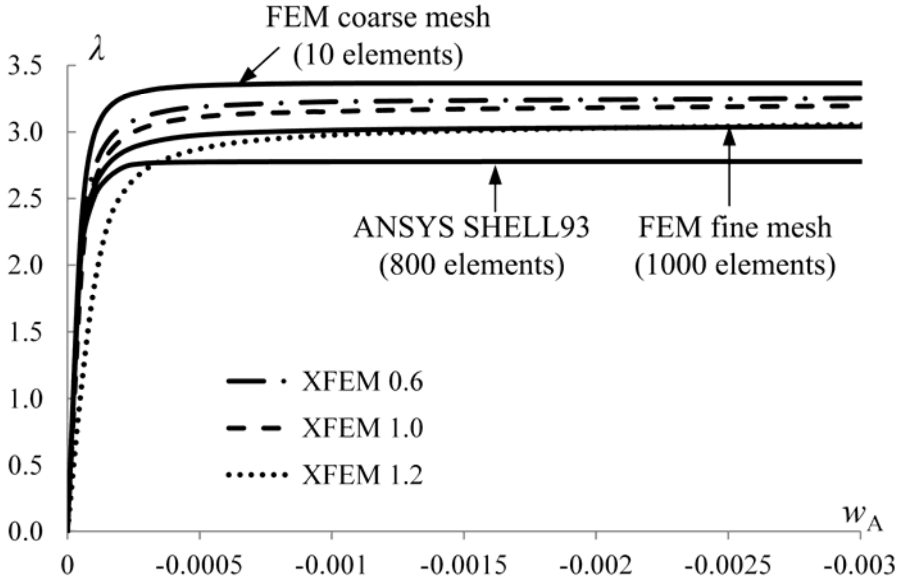

Figure 25 The equilibrium paths obtained for Example 2 with variation of l_{ns2}

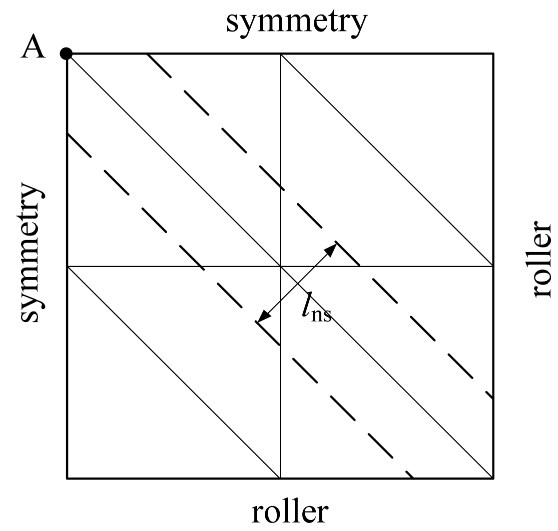

a) Mesh1 scheme

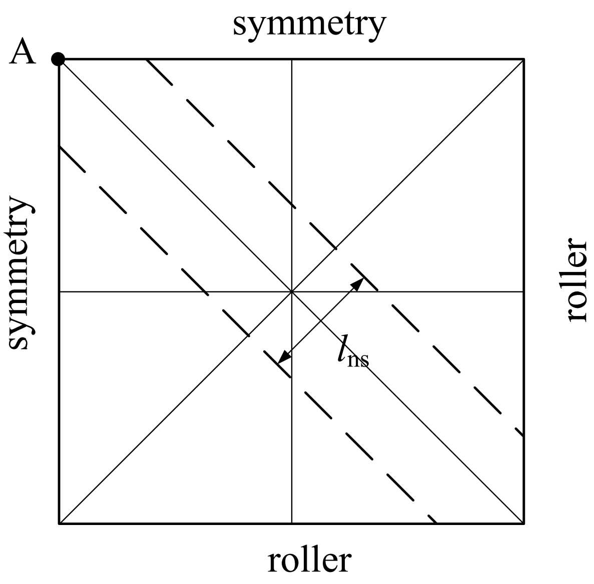

b) Mesh2 scheme

Figure 26 Example 3: A square plate with roller supports at the four edges

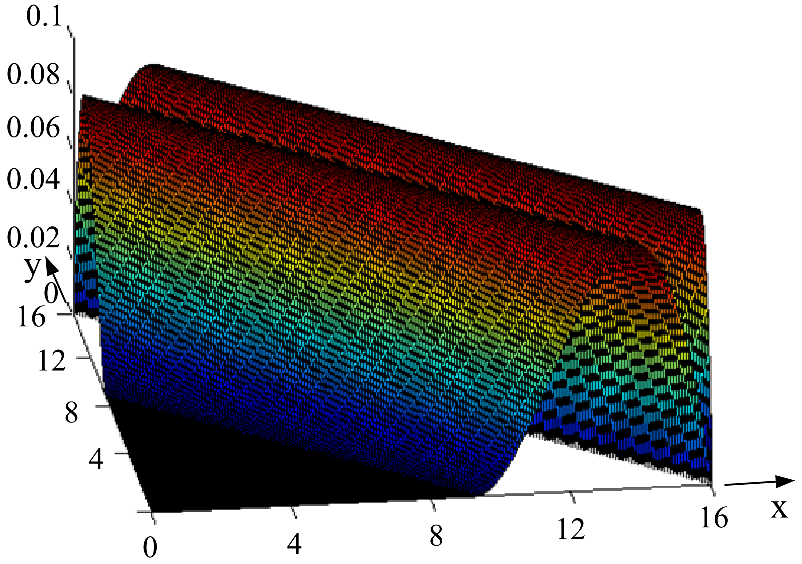

a) The 3D surface of the enrichment for deflection in Example 3

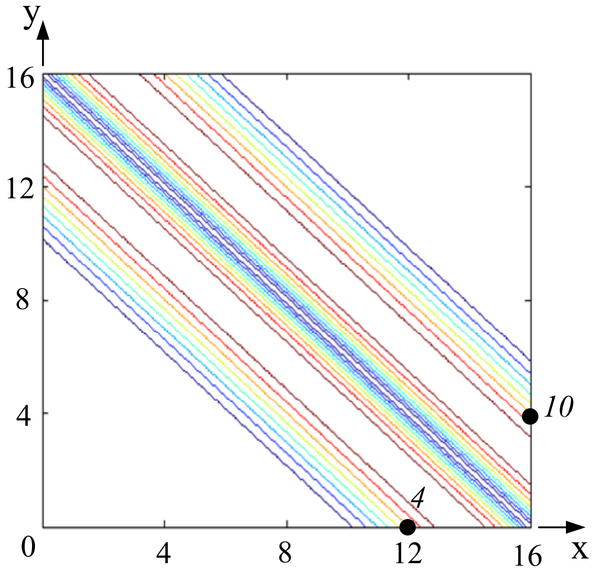

b) The contour of the enrichment for deflection in Example 3

Figure 27 The plot of the enrichment for deflection in Example 3 which shows an interelement C_0 continuity

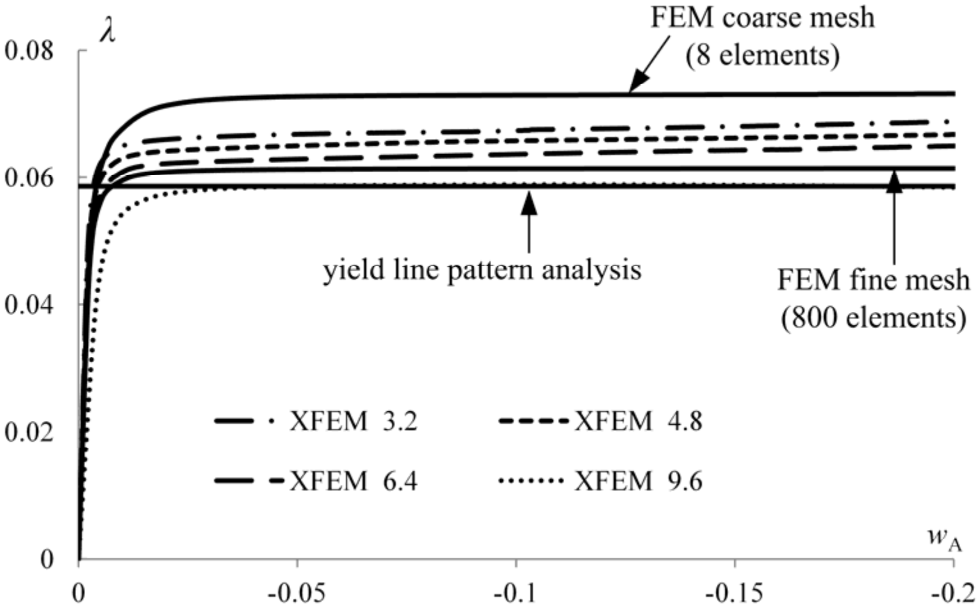

Figure 28 The equilibrium paths obtained for Example 3 using mesh1

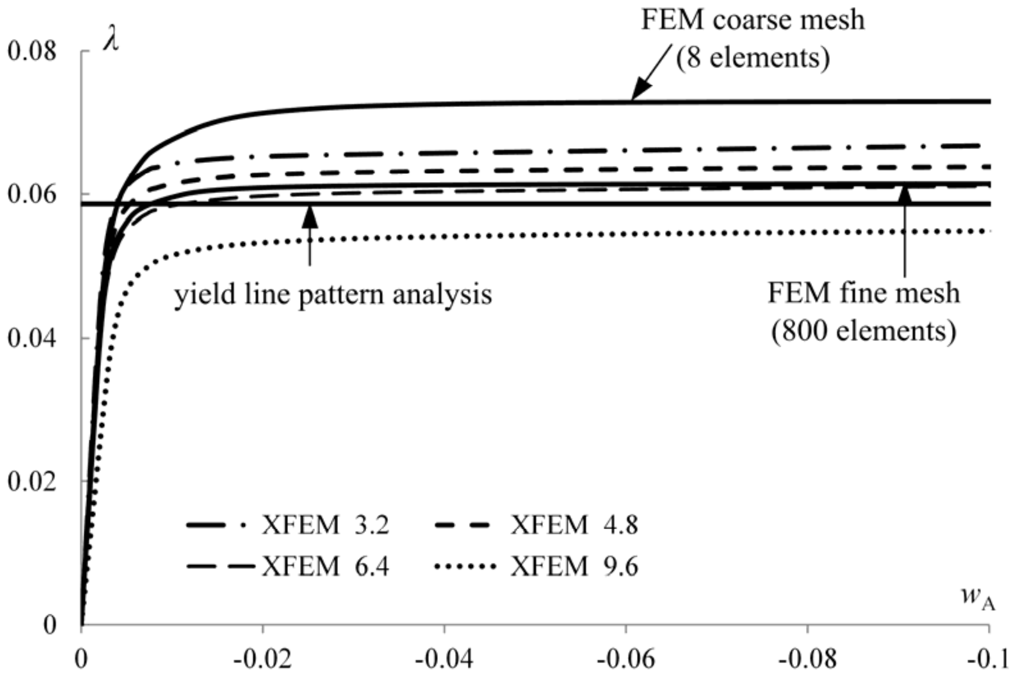

Figure 29 The equilibrium paths obtained for Example 3 using mesh2

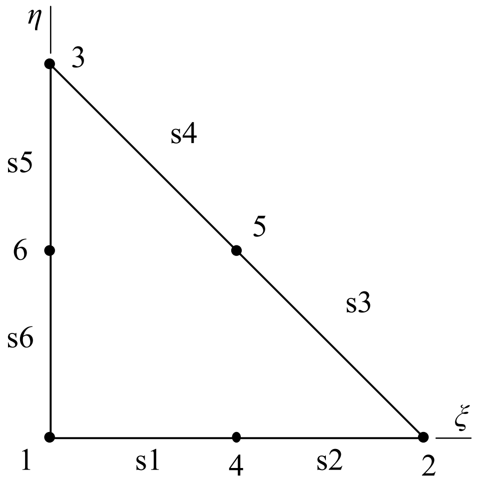

Figure A1 The line segment of an element

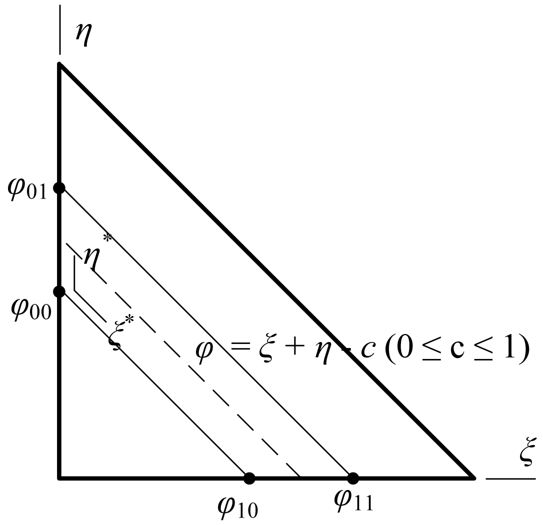

Figure B1 The yield line parallel to the hypotenuse

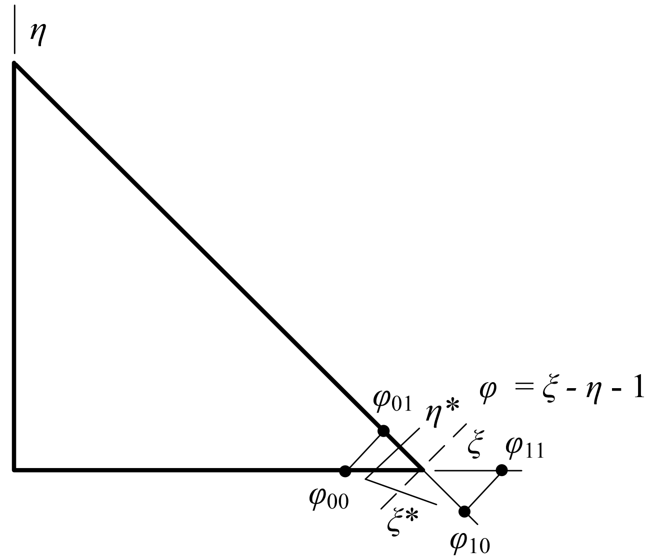

Figure B2 the yield line perpendicular to the hypotenuse (1)

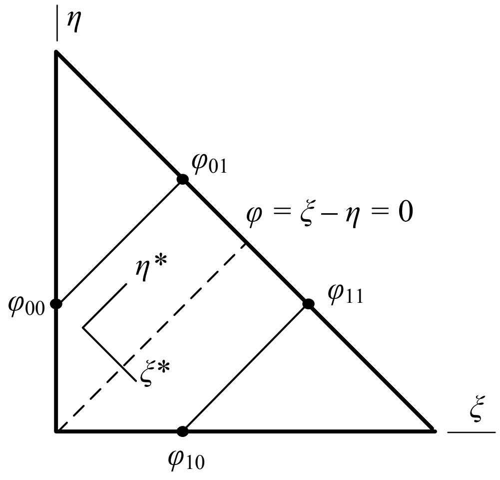

Figure B3 The yield line perpendicular to the hypotenuse (2)